



Helicon Double Layer Thruster Concept for High Power NEP Missions Final Report

Authors: Nicolas Plihon, Pascal Chabert, Jean-Luc Raimbault

Affiliation: Laboratoire de Physique et Technologie des Plasmas, CNRS-
Ecole Polytechnique

ESA Research Fellow/Technical Officer: Roger Walker

Contacts:

Pascal Chabert

Tel: +33 1 69 33 32 34

Fax: +33 1 69 33 30 23

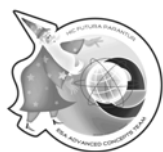
e-mail: chabert@lptp.Polytechnique.fr

Roger Walker

Tel: +31(0)715653349

Fax: +31(0)715658018

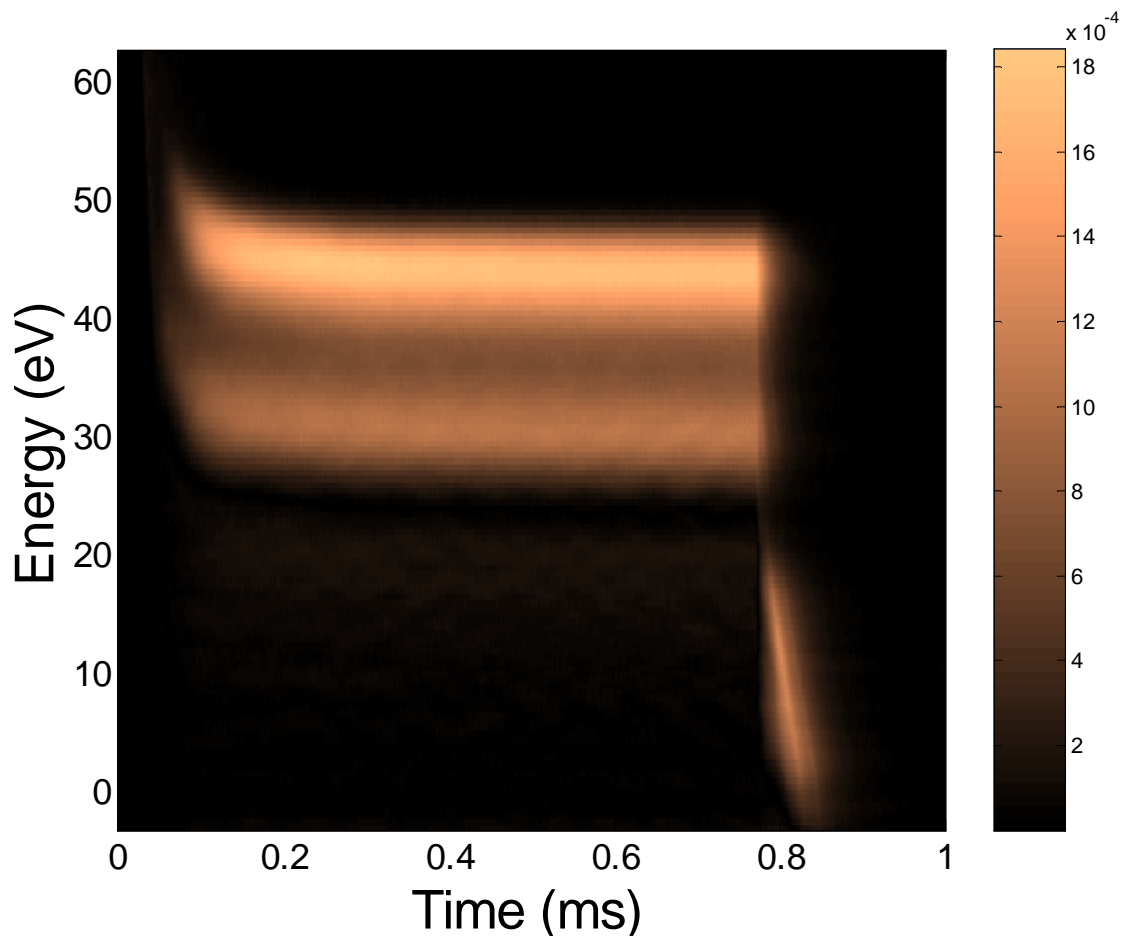
e-mail: act@esa.int



Available on the ACT website
<http://www.esa.int/act>

Ariadna ID: 04/3101
Study Duration: 4 months
Contract Number: 18852/05/NL/MV

Helicon Double Layer Thruster Concept for High Power NEP Missions Final report



Nicolas Plihon, Pascal Chabert and Jean-Luc Raimbault
Laboratoire de Physique et Technologie des Plasmas
CNRS-Ecole Polytechnique

Helicon Double Layer Thruster Concept
for High Power NEP Missions
Final report

Nicolas Plihon, Pascal Chabert and Jean-Luc Rimbault
Laboratoire de Physique et Technologie des Plasmas
CNRS-Ecole Polytechnique

January 23, 2006

Contents

1	Introduction	5
1.1	Space propulsion requirements	5
1.2	The ANU Helicon Double Layer Thruster (HDLT) Concept	5
1.2.1	General overview	5
1.2.2	Summary of the ANU group results on the HDLT	6
1.3	The LPTP Helicon reactor and diagnostics	8
1.3.1	The reactor	8
1.3.2	Diagnostics: electrical probes	8
2	Helicon plasma theory	15
2.1	Helicon waves	15
2.1.1	Wave propagation parallel to B_0	15
2.1.2	Off axis propagation	18
2.2	Antenna coupling and boundary conditions	19
2.2.1	Boundary conditions in cylindrical geometry	19
2.2.2	Antenna coupling	20
2.3	Ionization efficiency	22
2.4	E→H→W transitions	24
2.4.1	Capacitive mode (E)	25
2.4.2	Inductive mode (H)	25
2.4.3	Helicon modes (W)	26
2.4.4	E→H→W transitions	28
3	Double layer general theory	31
4	HDLT	37
4.1	Experimental evidence of Double Layer formation	37
4.2	Influence of the magnetic field strength	39
4.3	Influence of the gas pressure	40
4.4	Influence of the rf power	41
4.5	Ignition of the electropositive double layer	42
4.6	Influence of the boundary conditions	42
4.7	Limitations for propulsion testing	44

5	The Electronegative Double Layer Concept	49
5.1	Stable double layers	49
5.1.1	Experimental evidence of a double layer potential structure with Langmuir probes	49
5.1.2	Beam measurement in the downstream region	52
5.2	Transition toward unstable operation	54
5.3	Theory	56
5.3.1	Model assumptions	56
5.3.2	Boundary conditions	58
6	Conclusions	63
6.1	Estimation of specific impulse and thrust	63

Chapter 1

Introduction

1.1 Space propulsion requirements

The challenge for space propulsion is to achieve very high exhaust velocities in order to reduce the total propellant burden and therefore the spacecraft mass. Since a rocket-propelled spacecraft in free flight receives its acceleration from expelling mass (the propellant), its equation of motion is derived from momentum conservation

$$m\dot{v} = \dot{m}v_g \quad (1.1)$$

where m is the total mass of the spacecraft at a given time, \dot{v} its acceleration, v_g is the exhaust velocity of the propellant (relative to the spacecraft) and \dot{m} is the rate of change of the spacecraft mass due to mass expulsion. Integration of (1.1) for constant exhaust velocity gives the rocket equation,

$$\Delta v = v_g \ln \frac{m_0}{m_f} \quad (1.2)$$

which tells us that to increase the spacecraft velocity by Δv during a given period of acceleration, v_g has to be as high as possible in order to save propellant (m_0 is the initial mass and m_f is the final mass). The propulsion community usually uses two quantities to qualify a thruster, the thrust $T = \dot{m}v_g$, and the specific impulse $I_s = v_g/g_0$ where $g_0 = 9.81 \text{ ms}^{-2}$ is the gravity constant at sea-level. Deep-space or near earth planets (NEP) explorations require large Δv and therefore high specific impulse.

1.2 The ANU Helicon Double Layer Thruster (HDLT) Concept

1.2.1 General overview

The Plasma Research Laboratory (PRL) at the Australian National University has discovered a new phenomenon, an electric double layer in an expanding plasma, which needs to be further modelled and diagnosed. So far, there is no theoretical explanation for the formation of the double layer which only develops when a strongly diverging magnetic field is generated. The plasma is created by an helicon source, the principles of which are discussed in details in chapter 2, and then expands in the magnetized diffusion chamber where the double

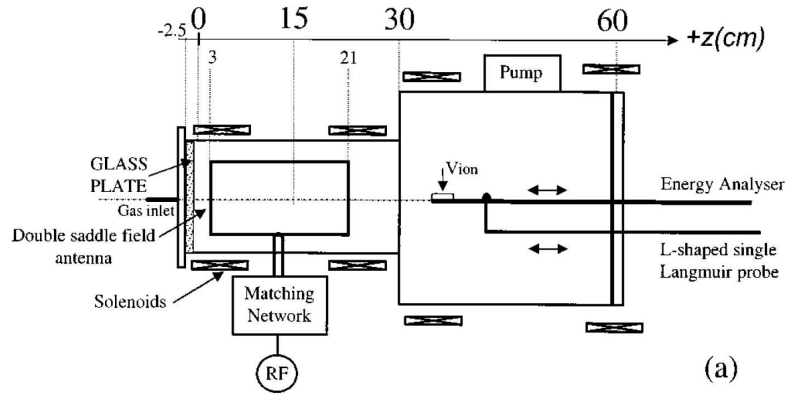


Figure 1.1: Schematic of the Chi-Kung reactor at PRL, Canberra (from [1])

layer is formed. A double-layer is a region of abrupt potential drop where quasi-neutrality is violated. The general theories of double-layers will be reviewed in chapter 3. This potential structure accelerates positive ions to the low-potential region, thus forming a supersonic beam. The double layers have great scientific relevance to solar flare disruptions, the solar wind and ionospheric charged particle acceleration. It seems also possible to further develop the phenomenon to be used as a new form of space plasma propulsion. The double-layer (electric) thrusters would not require high-current cathode, acceleration grids or neutraliser; a great advantage compared to existing electric thrusters which have limited lifetime. This concept has been evaluated and the results are summarized in this report.

1.2.2 Summary of the ANU group results on the HDLT

The SP3 (Space Plasma and Processing Plasma) group at the PRL has led an extended experimental [1, 2, 3, 4, 5] work plan on current-free double layers in an expanding magnetised plasma. Most of the results have been carried out in the Chi-Kung reactor which is schematically shown in fig 1.1, and has roughly the same size as the LPTP Helicon reactor.

The experimental requirements for Double Layer creation, according to the Australian group results, are:

- Strongly diverging static magnetic field (only the source coils are d.c. supplied)
- High amplitude of the static magnetic field (above 60 G, with a typical operational regime around 150 G)
- Very low gas pressure (in Argon the pressure-window for double layer existence is [0.2;1] mTorr)
- Fully insulated source chamber (no experimental evidence of D.L. occurrence with grounded parts in the source chamber has been published)

This Double Layer has been extensively studied over the past few years and the following characteristics, from experimental results, can be drawn (for an Ar plasma):

- Potential drop of about $3 T_e$, with T_e the electron temperature (that is a potential drop of about 25 V at 0.2 mTorr), occurring over a few Debye length (less than 1 cm which is about 50 Debye lengths). Since the electron temperature is inversely proportional to the gas pressure, the potential drop increases with decreasing pressure
- A plasma forms downstream of the double layer, with a density around $10^{16} m^{-3}$ for a 250W rf power, and a plasma potential around 25-30 V.
- The source tube might charge itself, such that the source plasma potential may reach 60 to 80 V.
- A supersonic ion beam at about twice the Bohm speed (which is about $5000 ms^{-1}$) is generated in the downstream region.
- The divergence of the beam has been measured to be only a few degrees. However, the measurements also show a beam density drop off going away from the DL, which is surprising (see our results in this report).
- The ion beam density relative to the downstream plasma density is about 0.2 at about 10 cm downstream of the double layer.

A number of experimental evidence of a supersonic beam, associated to the double layer formation, have been obtained when a strongly diverging magnetic field is present. The diagnostics used for probing the potential structure, particle densities, and particle energy distribution functions are: Langmuir probes (intrusive method), retarding Field Energy Analysers (non D.L. intrusive but plasma intrusive method), and Laser Induced Fluorescence (non intrusive method but very poor signal-to-noise ratio). These evidence have been obtained both at PRL (ANU) in the WOMBAT reactor (50 cm long, 18 cm diameter source and 2 m long, 1 m diameter diffusion chamber) [6], and at West Virginia University in the HELIX, a large and highly magnetized (static field up to 600 G) [7] experiment.

Numerical simulations are also currently developed at PRL by A. Meige using a Particle In Cell method and reproduce the main features of the D.L. with a diverging magnetic field [8, 9].

1.3 The LPTP Helicon reactor and diagnostics

1.3.1 The reactor

The LPTP helicon reactor is shown schematically in figure 1.2, and a picture of the entire experiment is shown on figure 1.3. It consists of a source chamber sitting on top of a 32 cm diameter diffusion chamber. This chamber is terminated by a movable plate, introduced through the bottom of the diffusion chamber, such that the diffusion chamber length can be varied between 0 and 26 cm. The source is a 14 cm diameter, 30 cm long and 0.9 cm thick pyrex cylinder surrounded by a double saddle field type helicon antenna [10]. The fan-cooled antenna is powered through a close-coupled L-type matching network by an rf power supply operating at 13.56 MHz and capable of delivering up to 2 kW forward power. The time-averaged input power was recorded as the difference between the time-averaged forward and reflected powers. The pyrex cylinder is housed in an aluminum cylinder of 20 cm diameter and 30 cm long. A metal grid attached to the other end of the source tube confines the plasma and separates it from a turbo-molecular pump that routinely maintains base pressures of 10^{-6} mbar. This grid can either be electrically isolated or be dc connected to the ground, which may make a big difference for the HDLT operation. The source and diffusion chambers are equipped with four coils to produce a static magnetic field of 0-200 Gauss. The discharge was run in pure Ar and in Ar/SF₆ mixtures. The partial gas pressures of Ar and SF₆ were determined by controlling the flows.

The main differences between the LPTP reactor and Chi-Kung reactor at Canberra are the following:

- The pump is placed on the side of the diffusion chamber on Chi-Kung, while at the top of the source chamber at LPTP.
- The source chamber is ended by a pyrex plate on Chi-Kung, while at the LPTP source is terminated by a grid, which can be either floating or dc connected to ground.

The influence of the boundary conditions are experimentally investigated and conclusions are given in this report.

1.3.2 Diagnostics: electrical probes

Langmuir probes

Measurements reported here were made both along the revolution axis (z axis) and along the radius of the median plane (r axis) of the plasma. The plasma parameters are determined using two types of electrostatic probes, shown on figure 1.8. The first is a nickel planar probe having a guard ring biased at the same (negative) potential as the probe, to measure the real saturated positive ion current. The diameter of the collecting area is 4 mm and the diameter of the outer ring is 8 mm. The second is a passively compensated Langmuir probe [11], of 0.25 mm diameter and 6 mm long platinum wire tip. For stationary plasmas and time-averaged measurements during the instability (occurring in the electronegative case), the plasma potential, the electron density and the electron temperature were deduced from the I(V) characteristics of the cylindrical probe using a Smartsoft data acquisition system [12]. The electronegativity, $\alpha = n_-/n_e$, and consequently the ion densities (electro-neutrality

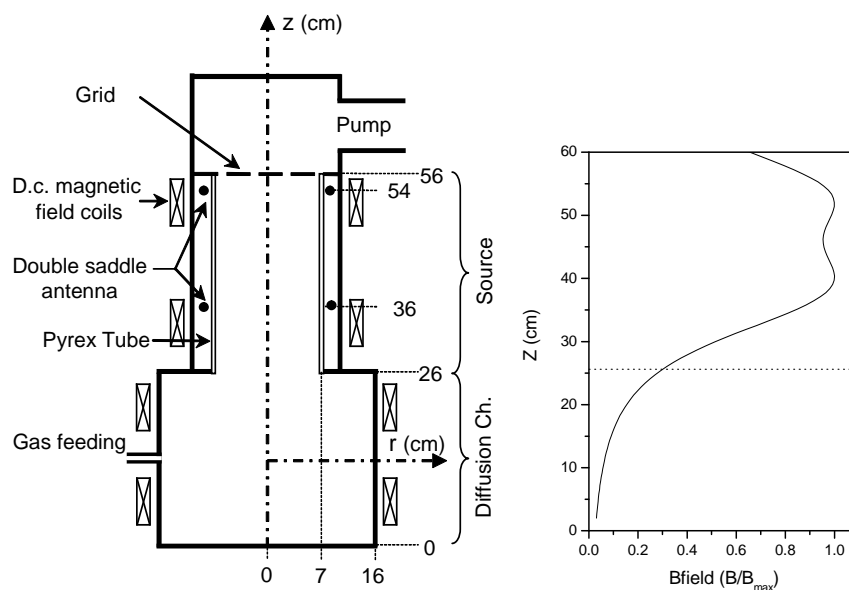


Figure 1.2: Schematic of the LPTP helicon reactor and calculated static magnetic field amplitude used in pure Argon at low pressure



Figure 1.3: Picture of the LPTP helicon reactor



Figure 1.4: Dense plasma in the expanding chamber of the helicon source

$n_+ = n_- + n_e$ was assumed), were measured according to the double-probe technique described in [13]. This technique, which relies on the theory developed in [14], allows to deduce α from the ratio of the cylindrical probe current at the plasma potential to the positive ion saturation current measured by the planar probe, $R = I(V_p)/I_{\text{sat}+}$. It requires an estimation of the ratio of the electron temperature to the negative ion temperature $\gamma = T_e/T_-$ and the positive ion mass m_+ , both difficult to measure in the gas mixture studied here. We chose $\gamma = 15$, as is commonly thought to be a reasonable value in low pressure electronegative discharges, $m_+ = 40$ since (i) Ar^+ may be dominant since we used small percentages of SF_6 in argon (ii) we expect a fairly high dissociation degree of SF_6 and therefore SF_x^+ ions with $x \ll 6$ (low mass ions). As a consequence of these estimations, the absolute values of α should be regarded as indicative. However, we believe that spatial gradients of α , or relative variations with operating conditions (pressure, power, mixture) are correctly captured by the technique.

Retarding Field Energy Analyzer

We have developed a retarding field energy analyzer consisting of four grids and a collector plate [15, 16, 17, 18]. The schematic of the RFEA is shown on figure 1.5

The analyzers were differentially pumped. They were composed of four grids made of nickel wires of 11 microns in diameter spaced by 40 microns; each grid had a 60 percent transparency. The entrance grid was grounded, a second grid was biased at -50 V to repel the electrons, the third grid was used to select the ion energy by scanning the voltage from 0

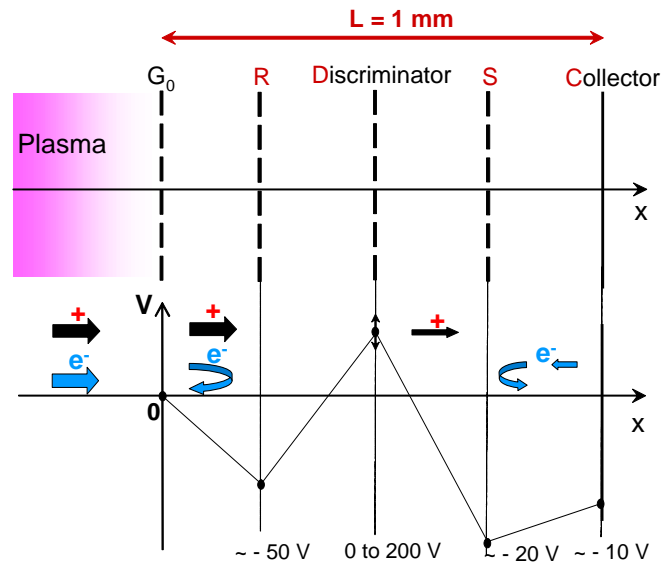


Figure 1.5: Schematic of the four grids retarding field energy analyzer

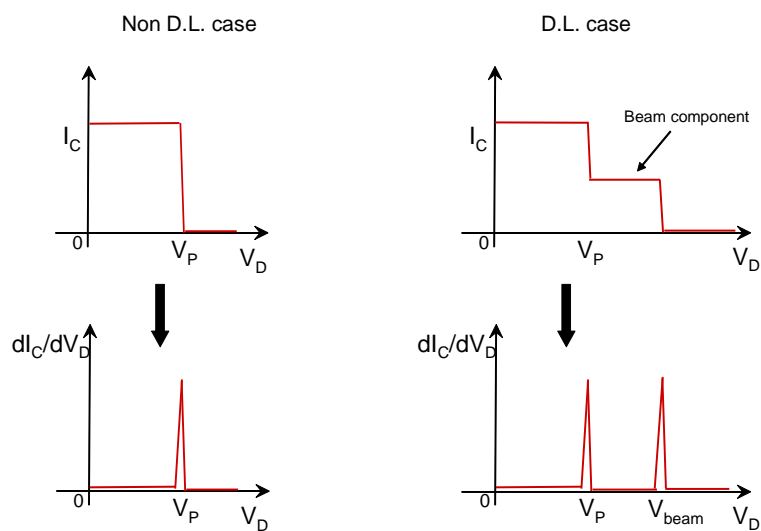


Figure 1.6: Schematic of the I-V characteristics analysis; no DL case and DL case

to 200 V, and a fourth grid was inserted before the collector in order to minimize the effect of secondary electrons [16]. The grids were spaced by 0.25 mm so that the total system length was about one millimeter. The ion current to the collector was recorded as a function of the dc voltage applied to the discriminator. When assembled, the analyzer is 35 mm long by 50 mm in diameter and the plasma particles enter the analyzer through a 2 mm hole in a 0.3 mm thick stainless steel orifice plate, in electrical contact with the analyzer housing, which is connected to the grounded diffusion chamber of the reactor.

The collected current I_c when the discriminator voltage is V_d :

$$I_c(v_0) = qAT^4 \int_{v_0}^{\infty} v f(v) dv \quad (1.3)$$

with $v_0 = \sqrt{\frac{2qV_d}{M_+}}$

with q the electrical charge, A the collecting surface, T the grid transparency, v_0 the speed of the ion accelerated by a grid at potential V_d and M_+ being the positive ion mass. The ion energy distribution function (IEDF) is then computed as $-\frac{dI_c}{dV_d}$. The ion distribution function is centered around the plasma potential with a dispersion due to the device resolution (see figure 1.6). We processed a best fit using a gaussian function, with the maximum of the gaussian being the plasma potential. Working out the ion saturation Γ_+ (the current measured for discriminator voltages below the plasma potential) it is possible to compute the ion density n_+ via the formula $\Gamma_+ = qAT^4vn_+$, v being the speed of the collected ions (which is called the Bohm speed $\sqrt{\frac{kT_e}{M_+}}$).

In the case of a measurement downstream the double layer, a double bumped IEDF is expected, with one bump centered at the plasma potential, and one bump corresponding to a ion beam accelerated within the double layer. Then the ion saturation current has got two components: The first one is due to the ion beam, which speed depends on the D.L. strength, and the second one is due to the local ions (generated in the downstream plasma), which can be interpreted similarly to the case described above (see figure 1.6).

The figure 1.7 shows a picture of our RFEA design, to be inserted from the bottom of the diffusion (expanding) chamber.



Figure 1.7: Pictures of the RFEA



Figure 1.8: Pictures of the Langmuir (left) and planar (right) probes

Chapter 2

Helicon plasma theory

2.1 Helicon waves

A large part of the material used in this report was taken from a very good review on helicons published by Boswell and Chen in IEEE transactions on Plasma Science [19],[20]. Helicon waves are part of a bigger group of waves called "whistlers", which were first observed during the first world war. Low frequency signals, looking like whistles, were detected by soldiers trying to intercept enemy communications. The possible origin of these signals was explained later. The lightning flashes at one end of earth generate a burst of waves (broad frequency spectrum around the kHz) in a short time. These waves propagate along the earth magnetic field lines at a speed that depends on the frequency (low frequencies propagate slowly). The dispersion is due to the anisotropy of the ionosphere refraction index. The signals received at the other end of earth last for few seconds and look like a whistle due to the effect produced by a short sound (about 2 seconds) with a decaying frequency. It should be noted that whistlers propagation in the ionosphere would not be possible without the earth magnetic field. Indeed, low frequency waves (having $\omega < \omega_{pe}$, the ionosphere plasma frequency) cannot propagate in non magnetized plasmas.

Helicon reactors, based on the propagation of helicon waves to produce high density plasmas, are used in various applications including plasma processing [21], [22]. A fully ionized argon plasma was obtained in the core of a cylinder by Zhu and Boswell [23]. Several other studies have emphasized the ionization efficiency of helicon or whistler waves [24],[25]. In the following, we will present the principles of plasma reactors. We will first briefly describe the various kind of waves existing in magnetized plasmas before focusing on helicons.

2.1.1 Wave propagation parallel to B_0

In this section we establish the dispersion relation of an electromagnetic wave propagating along (parallel to) a constant magnetic field B_0 in an infinite magnetized plasma. The anisotropic dielectric tensor is obtained from the electron momentum conservation equation and linearized Maxwell's equation for small perturbations. For the collisionless (low pressure, non resistive) case with the wave number k parallel to B_0 , we obtain two types of waves having the following dispersion relation:

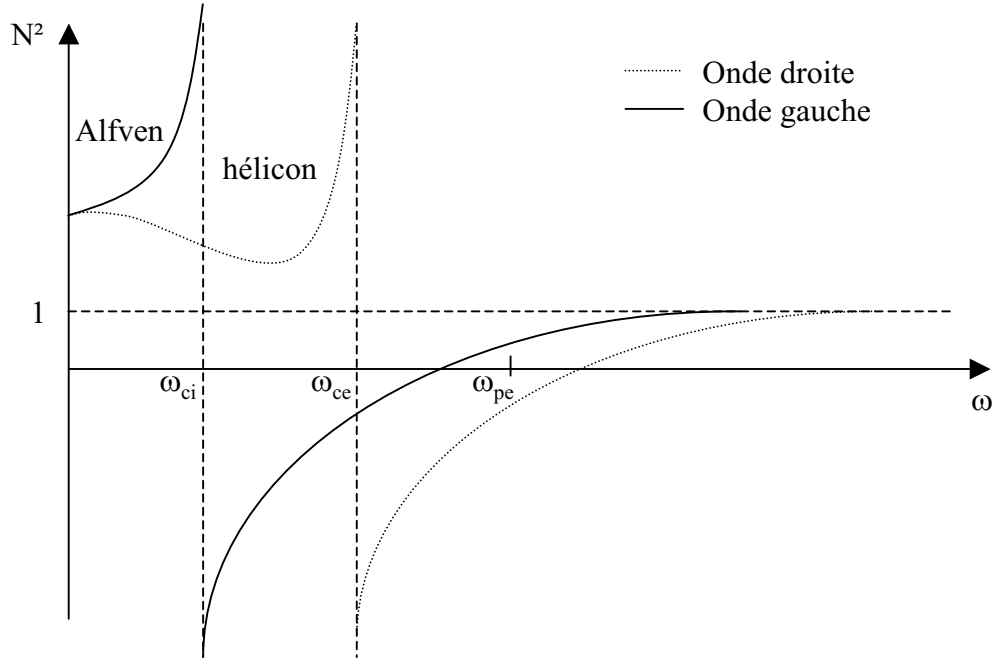


Figure 2.1: Dispersion diagram for the LHP and RHP polarized waves propagating parallel to B_0 for $\omega_{ce} \ll \omega_{pe}$

$$N_D^2 = \frac{k^2 c^2}{\omega^2} = 1 + \frac{\omega_{pe}^2 \left(1 + \frac{\omega_{ci}}{\omega_{ce}}\right)}{\omega \omega_{ce} \left(1 + \frac{\omega_{ci}}{\omega} - \frac{\omega}{\omega_{ce}} - \frac{\omega_{ci}}{\omega_{ce}}\right)} \quad (2.1)$$

$$N_G^2 = \frac{k^2 c^2}{\omega^2} = 1 - \frac{\omega_{pe}^2 \left(1 + \frac{\omega_{ci}}{\omega_{ce}}\right)}{\omega \omega_{ce} \left(1 - \frac{\omega_{ci}}{\omega} + \frac{\omega}{\omega_{ce}} - \frac{\omega_{ci}}{\omega_{ce}}\right)} \quad (2.2)$$

where ω_{ce} is the electron cyclotron frequency, ω_{ci} is the ion cyclotron frequency, and ω_{pe} is the electron plasma frequency. The first wave (dispersion relation given by 2.1) is called the right hand polarized wave, since the electric field E rotates clockwise if B is seen from behind. The second wave (dispersion relation given by 2.2) is called the left hand polarized wave, since the electric field E rotates anti-clockwise if B is seen from behind.

The dispersion diagram is shown on figure 2.1 where we have considered the case $\omega_{ce} \ll \omega_{pe}$. With this representation, $N^2 < 0$ indicates that the waves are evanescent, i.e. they are not propagating waves. The cut off frequencies are obtained for $N^2 = 0$ and the resonances are obtained for $N^2 \rightarrow \infty$.

The electric field for the left hand polarized wave rotates in the same direction than ions around the magnetic field, thus the resonance is at ω_{ci} . On the contrary, The electric field for the right hand polarized wave rotates in the same direction than electrons around the

magnetic field, and therefore the resonance is at ω_{ce} . As shown on the diagram, the waves become evanescent above their respective resonance frequencies. As ω approaches ω_{pe} , the waves become propagating again and when ω goes to infinity, the phase velocity approaches the speed of light (since $N^2 \rightarrow 1$).

Helicons are low frequency right hand polarized waves. We therefore restrict our study to the domain $\omega < \omega_{ce}$. We also consider $\omega_{ce} \ll \omega_{pe}$, $\omega_{ci} \ll \omega_{ce}$ and $\omega \ll \omega_{pe}$, which gives the following dispersion relation (from 2.1):

$$N_D^2 = \frac{\omega_{pe}^2}{\omega\omega_{ce} \left(1 + \frac{\omega_{ci}}{\omega} - \frac{\omega}{\omega_{ce}}\right)} \quad (2.3)$$

From this expression, we identify three types of waves which are important in various fields: space plasma, magnetic fusion energy and plasma processing. The difference will mainly come from the frequency, i.e. from the dominant terms in equation 2.3.

Alfven compressional waves

If we consider frequencies near ω_{ci} , then ω/ω_{ce} is negligible and we obtain the following dispersion relation:

$$N^2 = \frac{\omega_{pe}^2}{\omega_{ce}(\omega_{ci} + \omega)} \quad (2.4)$$

For very low frequencies ($\omega \ll \omega_{ci}$), we obtain the so-called Alfven waves which are not dispersive since the phase velocity is independent of frequency. The phase velocity is then called Alfven velocity and is given by:

$$v_\varphi = \frac{c}{N} = v_A = \frac{c}{\omega_{pe}} \sqrt{\omega_{ci}\omega_{ce}} = c \frac{\omega_{ci}}{\omega_{pi}} \quad (2.5)$$

Alfven waves exist in two forms: compressional and torsional. The first modify the magnetic field lines whereas the second compress them. The compressional waves are used in Tokamaks reactors for ion heating (typically 60 MHz).

Electron cyclotron waves

If we consider frequencies near ω_{ce} , we can neglect ω_{ci}/ω and the dispersion relation becomes :

$$N^2 = \frac{\omega_{pe}^2}{\omega\omega_{ce} \left(1 - \frac{\omega}{\omega_{ce}}\right)} \quad (2.6)$$

The index N^2 is minimal at $\omega = 0.5\omega_{ce}$, where the phase velocity is maximal. The wave nature is different depending whether $\omega > 0.5\omega_{ce}$ or $\omega < 0.5\omega_{ce}$ (see Boswell and Chen for details). The electron cyclotron waves (at $\omega > 0.5\omega_{ce}$) are used for electron heating in tokamaks. They are also used in plasma processing reactors called ECR (for Electron Cyclotron Resonance). The excitation frequency is usually 2.45 GHz which fixes the magnetic field at 875 Gauss to be at the resonance ($\omega = \omega_{ce}$).

Helicon waves

Helicon waves are at the low frequency limit of electron cyclotron waves (i.e. $\omega < 0.5\omega_{ce}$). The frequency is sufficiently high so that ions do not respond to the field, and sufficiently low so that electron inertia is small, i.e. $\omega_{ci} \ll \omega \ll \omega_{ce}$. The name "helicon came from

the fact that electrons rotate with the electric field in a helicoidal motion. The dispersion relation is given by :

$$N^2 = \frac{\omega_{pe}^2}{\omega\omega_{ce}} \quad (2.7)$$

The helicon reactor are designed to allow the helicon wave propagation. For the typical conditions of a magnetized argon plasma, i.e. $n_e = 10^{12} \text{ cm}^{-3}$ and $B_0 = 70 \text{ Gauss}$ ($B_0 = 7 \times 10^{-3} \text{ Tesla}$) we obtain : $\omega_{ce} = eB_0/m_e = 1.25 \times 10^9 \text{ Hz}$, $\omega_{ci} = eB_0/m_+ = 1.67 \times 10^4 \text{ Hz}$, $\omega_{pe} = 5.7 \times 10^{10} \text{ Hz}$. The conventional excitation frequency is 13.56 Mhz, which means that $\omega = 2\pi f = 8.5 \times 10^7 \text{ Hz}$. Therefore we meet the following conditions $\omega_{ci} \ll \omega \ll \omega_{ce} \ll \omega_{pe}$, required for the helicon wave propagation.

Since the plasma in the reactor is spatially limited, the wave propagation is more complex than what have been described above. The boundary conditions impose both standing waves and off axis propagation, that is the wave does not propagate parallel to B_0 . In the following section we briefly describe off axis propagation.

2.1.2 Off axis propagation

In this section we analyse the wave propagation with an angle $\theta \neq 0$ relative to the magnetic field, in an infinite magnetized plasma. In that case, the dispersion relation for electron cyclotron waves is given by:

$$N^2 = 1 - \frac{\omega_{pe}^2}{\omega(\omega - \omega_{ce} \cos \theta)} \quad (2.8)$$

In the case of helicon waves, for $\omega_{ce} \ll \omega_{pe}$, the relation (2.8) becomes:

$$N^2 = \frac{\omega_{pe}^2}{\omega(\omega_{ce} \cos \theta - \omega)} \quad (2.9)$$

Note that at $\theta = 0$, we obtain the dispersion relation established before (see 2.6). When $\theta \neq 0$ the index is anisotropic. At a given frequency, there exists a limit angle for propagation defined as follow:

$$\cos \theta = \frac{\omega}{\omega_{ce}} \quad (2.10)$$

where there is a resonance. Using our typical value for the electron cyclotron frequency $\omega_{ce} = 1.25 \times 10^9 \text{ Hz}$ we obtain a phase velocity resonance cone at θ such that: $\cos \theta = \frac{\omega}{\omega_{ce}} = 0.068$ that is $\theta = 86.1^\circ$.

Since we are in an anisotropic medium, the wave energy does not propagate in the direction of the wave number. The direction of energy propagation as well as the group velocity direction are given by Pointing's vector. As for the phase velocity, there exists a resonance cone of angle θ for the group velocity. The calculation of this angle is complicated and is beyond the scope of this report (see Boswell and Chen for details). Since we are at low frequencies, $\omega < 0.5\omega_{ce}$ the value for this angle is $\theta = 19.28^\circ$.

As a summary, in an infinite magnetized plasma with a driving frequency $f = 13.56 \text{ MHz}$ and a magnetic field $B_0 = 70 \text{ Gauss}$, the helicon wave propagate within a cone of angle $\theta = 86.1^\circ$ relative to B_0 (wave number and phase velocity directions). However, the wave energy (the direction of the group velocity) propagates within a cone of angle $\theta = 19.28^\circ$. Therefore, energy transfer to electrons will mainly occur close to the direction of the magnetic field.

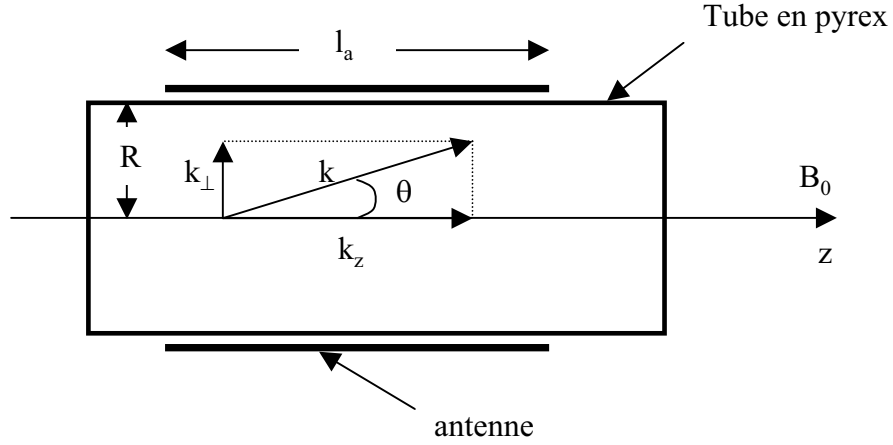


Figure 2.2: Schematic of the helicon antenna around the source tube, with wave numbers

2.2 Antenna coupling and boundary conditions

2.2.1 Boundary conditions in cylindrical geometry

The source tube is usually made of quartz or pyrex and is therefore a dielectric, i.e. the plasma boundaries are dielectric. The wave vectors are sketched on the figure 2.2.

The helicon wave can exist if three basic relations, listed below, are satisfied. The first relation is obvious:

$$k_{\perp}^2 + k_z^2 = k^2 \quad (2.11)$$

The second relation is the dispersion relation established previously for the general case, i.e. for the off axis propagation of the helicon wave (relation 2.9) with $\omega \ll \omega_{ce}$:

$$N^2 = \frac{k^2 c^2}{\omega^2} = \frac{\omega_{pe}^2}{\omega \omega_{ce} \cos \theta} \quad (2.12)$$

This relation can also be written as follow,

$$k k_z = \frac{e \mu_0 n_0 \omega}{B_0} \quad (2.13)$$

if we express the electron plasma frequency and the electron cyclotron frequency as a function of the electron density n_0 .

The third relation is imposed by the cylindrical geometry. The wave electric and magnetic fields have the following form:

$$E, B \sim \exp j (\omega t - k_z z - m \varphi) \quad (2.14)$$

where m is the azimuthal mode number. Chen [24] demonstrated that if the plasma density is constant along the radius, and if the electric field is zero at $r = R$, then we obtain the

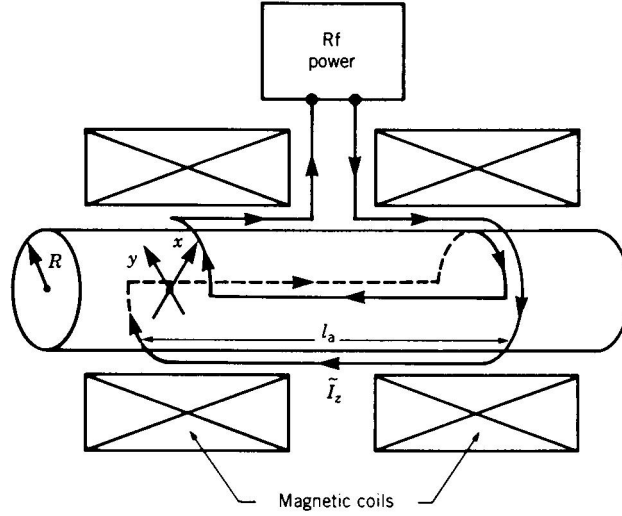


Figure 2.3: Boswell type antenna

following condition for the $m = 1$ mode:

$$kJ_1(k_{\perp}R) + k_z J_1'(k_{\perp}R) = 0 \quad (2.15)$$

where J_1 is the first order bessel function. This equation is solved numerically. It imposes a condition on the perpendicular wave number k_{\perp} . For a given radius, we always (i.e. whatever the value of k_z) have $2.4 < k_{\perp}R < 3.83$.

The three equations (2.11, 2.13 and 2.15) lead to an infinite number of solutions. However, the antenna will only excite a finite number of solutions, which will fix the last condition on the longitudinal wave number k_z . Therefore, for a given antenna geometry, we will find a discrete number (called n in the following) of values for k_z , each of them associated to a particular electron density n_0 . The antenna coupling mechanisms are analyzed in the next section, for the Boswell type antenna designed to excite the $m = 1$ azimuthal mode.

2.2.2 Antenna coupling

Helicon processing reactors may use two different antenna types: either antenna that excites the $m = 0$ or the $m = 1$ azimuthal modes. The Boswell type, exciting the $m = 1$ azimuthal mode, has been found to be the most efficient antenna in term of ionization. A schematic of this antenna is presented on figure 2.3.

The antenna coupling mechanisms are still poorly understood. It is usually proposed that a quasi-electrostatic electric field builds up between the two longitudinal ends of the antenna, due to the fact that the rf current circulates in opposite direction in the two antenna branch of length l_a . The length of the antenna is therefore critical since it will fix values for k_z . If we consider that the electric field perpendicular to z is a Dirac function, we have

$$E(z) = E_0 \Delta z \left(\delta \left(z + \frac{l_a}{2} \right) - \delta \left(z - \frac{l_a}{2} \right) \right) \quad (2.16)$$

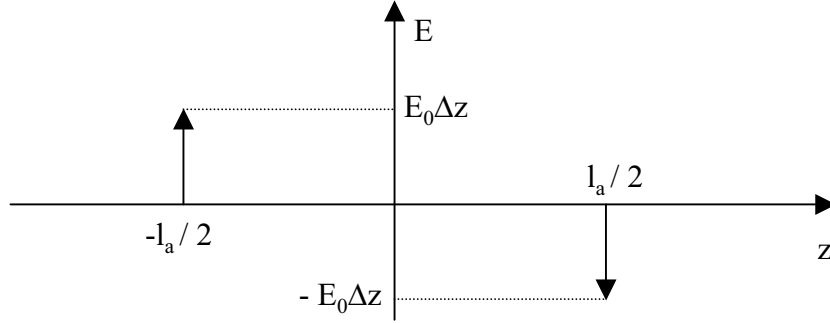


Figure 2.4: Electric field created by circulation of the rf current in the antenna

The electric field E is sketched on figure 2.4 as a function of z . Taking the Fourier transform, we obtain the electric field as a function of the longitudinal wave number k_z . The power coupled by the antenna is then proportional to the square of the electric field, leading to

$$E^2(k_z) = 4E_0^2(\Delta z)^2 \sin^2\left(\frac{k_z l_a}{2}\right) \quad (2.17)$$

The maximum of the power are therefore obtained for $k_z = \pi/l_a$, $k_z = 3\pi/l_a$, $k_z = 5\pi/l_a$ etc. and on the contrary, the minimum are obtained for $k_z = 0$, $k_z = 2\pi/l_a$ etc. The corresponding wavelength for the maximum will then be: $\lambda_z = 2l_a$, $\lambda_z = 2l_a/3$, $\lambda_z = 2l_a/5$ etc. We can now calculate the characteristic of each longitudinal mode n excited by this antenna, given typical values of $B_0 = 70$ G, $\omega = 85,2$ MHz, $R = 8$ cm, and $l_a = 20$ cm. the system is defined by four equations, the three relations obtained above 2.11, 2.13 and 2.15, and the condition on k_z :

$$\begin{aligned} k_z &= (2n + 1)\frac{\pi}{l_a} \\ k k_z &= 2.447 \times 10^{-15} n_0 \\ k J_1(k_\perp R) + k_z J'_1(k_\perp R) &= 0 \\ k_\perp^2 + k_z^2 &= k^2 \end{aligned} \quad (2.18)$$

The characteristics of each mode n are summarized in the following table:

n	k_z (m ⁻¹)	λ_z (cm)	k_\perp (m ⁻¹)	k (m ⁻¹)	θ	n_0 (cm ⁻³)
0	15.7	40.0	35.7	39.0	66.3	2.5×10^{11}
1	47.1	13.3	31.1	56.4	33.4	1.1×10^{12}
2	78.5	8.0	30.4	84.2	21.2	2.7×10^{12}
3	109.9	5.7	30.2	114	15.4	5.2×10^{12}
4	141.3	4.5	30.1	144.5	11.8	8.3×10^{12}

We see that the first mode appear for an electron density of $n_0 = 2.5 \times 10^{11}$ cm⁻³, and that higher densities are required for higher order modes ($n \geq 1$). It should also be noted

that this density depends upon the static magnetic field B_0 . If one wants to excite a mode at lower density, then B_0 should be smaller. On the contrary to get higher density, one should increase B_0 . The value of θ given in the table is the angle between the wave number and the static magnetic field. However, as mentioned above, the wave energy (direction of the group velocity) propagate within a small angle $\theta \approx 19^\circ$.

2.3 Ionization efficiency

In the previous sections we have defined the wave propagation characteristics and the antenna coupling. In a helicon source, the wave energy will be transferred to electrons to provide ionization. There are two different mechanisms for electron heating (i.e. for power dissipation of the wave). The first is called "ohmic" or collisional heating and the second is called "stochastic" or non-collisional heating. In the first case, the power dissipation is due to collisions of electrons on other particles, e.g. ions, electrons, or neutrals. If one consider the oscillation of an electron in a sinusoidal electric field (E at ω), the momentum conservation gives

$$m_e \frac{\partial v}{\partial t} = eE_0 \cos(\omega t) \quad (2.19)$$

The electron velocity is therefore given by :

$$v(t) = \frac{eE_0}{m_e \omega} \sin(\omega t) \quad (2.20)$$

From Ohm's law, we see that there is no power dissipation:

$$P_{diss} = \langle J \cdot E \rangle \propto \langle \cos(\omega t) \sin(\omega t) \rangle = 0 \quad (2.21)$$

However, if the electrons experience collisions during the motion, the dissipated power will not be zero. Equation 2.19 becomes:

$$m_e \frac{\partial v}{\partial t} = eE_0 \cos(\omega t) - m_e \nu v \quad (2.22)$$

where ν is the collision frequency. The velocity is now given by:

$$v(t) = \frac{eE_0}{m_e(\omega^2 + \nu^2)} \cos(\omega t + \theta) \quad (2.23)$$

with

$$\tan(\theta) = \omega/\nu \quad (2.24)$$

Therefore, the dissipated power is given by

$$P_{diss} = \langle J \cdot E \rangle \propto \langle \cos(\omega t) \cos(\omega t - \theta) \rangle \neq 0 \quad (2.25)$$

Indeed, we see that if $\nu \neq 0$ (then $\theta \neq \frac{\pi}{2}$) there exists a phase shift θ , function of the collision frequency ν , and the average is not zero. With this ohmic power dissipation, it should be noted that the power is mainly transferred to low-energy bulk electrons.

At low pressure, typically $P < 10$ mTorr, the collision frequency is too low to explain efficient electron heating (very high ionization degrees were observed in low-pressure helicon

plasmas [23]) and therefore non-collisional mechanisms are responsible for power absorption. Landau damping is a well known collisionless mechanism in which the wave is absorbed by electrons having velocities near the phase velocity v_φ . One can choose the phase velocity v_φ of the wave, by choosing the excitation frequency and/or the antenna length, such that 50 eV electrons absorb the wave. This energy (50 eV) is near the maximum of the ionization cross section, and therefore allow very efficient plasma production. Unfortunately, the maximum of the wave absorption is not obtained at 50 eV, but rather near the electron average energy, i.e. at much lower energy (Landau damping is maximum when the phase velocity equals the electron thermal velocity: $v_\varphi = v_{The}$). One therefore need to decide (when designing the antenna) between high landau damping heating low energy electrons (not efficient for ionization) or weak landau damping heating 50 eV electrons (efficient for ionization). The second choice is usually the best. However, other non-collisional mechanisms may exist. Degeling et Boswell [26] have shown by numerical simulation that electron trapping in the wave is dominating in some conditions.

In the following, we estimate the distance in which the wave is absorbed by two mechanisms: (i) collisional (ohmic), and (ii) Landau damping. These calculations have been made from Chen [24]. Each mechanism is defined by a collision frequency. The total "effective" collision frequency ν_{tot} is the sum of the real collision frequency (electron-ion, electron-neutral, etc.) and the effective Landau collision frequency:

$$\nu_{tot} = \nu_c + \nu_L \quad (2.26)$$

The effective Landau collision frequency is given by:

$$\nu_L = 2\sqrt{\pi}\xi^3 \exp(-\xi^2) \quad (2.27)$$

if $\xi \gg 1$, with

$$\xi = \frac{\omega}{\sqrt{2}k_z v_{th}} \quad (2.28)$$

and $v_{th} = \sqrt{kT_e/m_e}$. The electron-ion collision frequency is given by:

$$\nu_{ei} = 2.9 \times 10^{-12} n_0 Z \ln \Lambda T_e^{-\frac{3}{2}} \quad (2.29)$$

where $Z = 1$ is the ion charge, n_0 is the plasma density (expressed in m^{-3}) and T_e is the electron temperature. $\ln \Lambda$ is the Coulomb logarithm, and in general $\ln \Lambda = 10$. Choosing $T_e = 5$ eV, we obtain : $\nu_{ei} = 2.594 \times 10^{-12} n_0$ Hz.

The electron-neutral collision frequency for a $P = 1$ mTorr argon plasma with $T_e = 5$ eV, is about $\nu_m = 4.8 \times 10^6$ Hz. From these two expressions we see that electron-ion collisions dominate electron-neutral collisions if $n_0 > 2 \times 10^{12} cm^{-3}$ which is typical in high power operation of an helicon plasma.

The characteristic wave absorption length, along the z axis, is defined from the total collision frequency as follow:

$$\alpha_z = \frac{\omega_{ce}}{k_\perp \nu_{tot}} \quad (2.30)$$

if $k_\perp \gg k_z$, and

$$\alpha_z = \frac{2\omega_{ce}}{k_z \nu_{tot}} \quad (2.31)$$

if $k_{\perp} \ll k_z$. Finally, the energy of electrons interacting with the wave, when Landau damping dominates, is given by:

$$E_L = \frac{1}{2}m_e v_{\phi}^2 = \frac{1}{2}m_e \left(\frac{\omega}{k_z}\right)^2 \quad (2.32)$$

As mentioned above, low energetic electrons, typically $E_c = 2.5$ eV, are responsible for collisional damping. We can now calculate the absorption characteristics of each modes excited in our system (the absorption length is α_z :

n	k_z (m ⁻¹)	n_0 (cm ⁻³)	ν_L (s ⁻¹)	ν_c (s ⁻¹)	α_z (m)	E_L (eV)	E_c (eV)
0	15.7	2.5×10^{11}	2175	5.4×10^6	6.5	80	2.5
1	47.1	1.1×10^{12}	1.2×10^8	7.6×10^6	0.4	9.2	2.5
2	78.5	2.7×10^{12}	-	1.18×10^7	< 2.7	3.3	2.5
3	109.9	5.2×10^{12}	-	1.83×10^7	< 1.2	1.7	2.5
4	141.3	8.3×10^{12}	-	2.63×10^7	< 0.7	1.0	2.5

We see that the first mode is not efficiently absorbed by Landau or collisional damping since the typical absorption length is 6.5 m! In fact, other damping mechanisms (described by Degeling and Boswell [26]) occur since experimentally it has been shown that this mode was absorbed. The second mode ($n = 1$) is efficiently absorbed by Landau damping and higher order modes are efficiently absorbed by collisional processes (mainly electron-ion collisions). As a conclusion for this part, very efficient wave damping observed experimentally are due to collisionless mechanisms (Landau damping or electron trapping) at low-pressure low-density (typically 1 mTorr, $n_0 < 2 \times 10^{12}$ cm⁻³) and to collisional mechanisms at higher pressure and/or higher densities. The efficient damping explains the very high ionization efficiency.

2.4 E→H→W transitions

We have shown that helicon wave propagation requires a minimum plasma density. However, an helicon reactor can operate at low density (or low injected power), where the wave is not excited. Since there is a substantial voltage across the antenna, a fraction of the discharge power is also deposited capacitively, and this voltage drives a capacitive current in the plasma. In addition, the rf current flowing in the antenna (which behaves as a non resonant inductive coil) result in plasma creation within or near the coil by the induced rf electric field. The discharge can therefore exist in three different modes: the capacitive mode (E mode), for low power, the inductive mode (H mode), for intermediate power and finally the helicon mode (W) for high power. As the power is increased, transitions from capacitive to inductive to helicon modes (E→H→W) are observed.

The helicon discharge operation and the transitions can be simply modelled by doing electron power balance. It can be shown that the electron loss power is due both to collision within the plasma bulk and to kinetic energy loss at the wall. The loss power is given by:

$$P_{loss} = h_l n_e u_B A (E_c + E_e) \quad (2.33)$$

where n_0 is the plasma density, u_B is the Bohm velocity, A is the reactor surface, E_c is the energy loss per collisions (ionization, excitation, elastic etc.) and E_e is the kinetic energy

loss at the wall. $E_e = 2T_e$ for Maxwellian electrons, E_c and u_B depend on the electron temperature T_e which is a very weak function of the injected power. The loss power is therefore proportional to the electron density:

$$P_{loss} \propto n_e \quad (2.34)$$

The absorbed power is more complicated since it depends on the power absorption mechanism.

2.4.1 Capacitive mode (E)

The operation in capacitive mode is reasonably well understood. The mobile electrons, responding to the instantaneous electric fields produced by the rf driving voltage, oscillate back-and-forth within the positive space charge cloud of the ions. The massive ions respond only to the time-averaged electric fields. The electric field in the plasma bulk is weak, due to high electrostatic shielding by the sheath, but sufficient to produce significant ohmic heating. However, at low pressure the oscillating sheaths produce very efficient non-collisional stochastic heating. The absorbed power is therefore the sum of two terms and the power balance is given by:

$$P_{loss} = P_{ohm} + P_{stoc} \quad (2.35)$$

where P_{ohm} is the ohmic heating term (i.e. due to collisions in the bulk) and P_{stoc} is the stochastic term (i.e. due to the sheath dynamic). At low density, the absorbed power is independent of the plasma density. At higher density, both stochastic and ohmic heating terms decay with the plasma density, with the following scalings:

$$P_{ohm} \propto \frac{V_{rf}^2}{n_e} \quad (2.36)$$

$$P_{stoc} \propto \frac{V_{rf}^4}{n_e^2} \quad (2.37)$$

These relations (2.34, 2.36 and 2.37) allow to establish the operation diagram shown on figure 2.5. This diagram represents both absorbed and loss powers as a function of plasma density. The operating point is at the crossing of the two (loss and absorbed power) curves.

As mentioned above, the helicon discharge operates in the capacitive mode at low injected power.

2.4.2 Inductive mode (H)

An inductive discharge is usually created by application of radio-frequency power to a non-resonant inductive coil, resulting in the breakdown of the process gas within or near the coil by the induced rf electric field. The induced (evanescent) fields penetrate the plasma within a typical distance called the skin depth δ . We consider a low pressure collisionless plasma created by a N turns coil, and in a cylinder having $l > R$. The skin depth is given by:

$$\delta = \sqrt{\frac{m_e}{n_e e^2 \mu_0}} \quad (2.38)$$

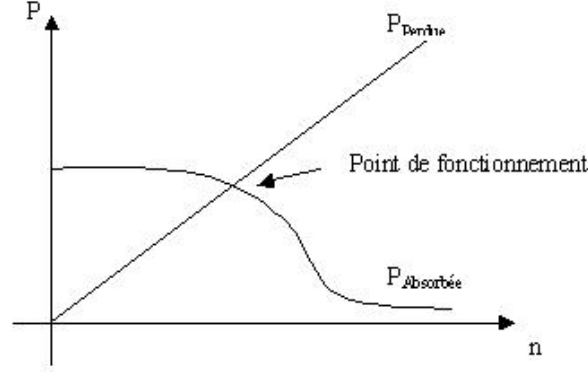


Figure 2.5: Absorbed and loss powers as a function of plasma density in the capacitive mode

The plasma effective conductivity, which takes into account collisions and stochastic processes (effective collision frequency ν_{eff}), is given by:

$$\sigma_{eff} = \frac{n_e e^2}{m_e \nu_{eff}} \quad (2.39)$$

For high density regime (where the skin depth is small compared to the cylinder radius), the absorbed power is given by :

$$P_{abs} = \frac{1}{2} N^2 \frac{2\pi R}{l \sigma_{eff} \delta} I_{rf}^2 \quad (2.40)$$

Combining equations 2.38, 2.39 and 2.40, we obtain the following scaling for absorbed power as a function of the plasma density:

$$P_{abs} \propto n_e^{-\frac{1}{2}} I_{rf}^2 \quad (2.41)$$

For the low density regime, the skin depth is large compared to the cylinder radius ($\delta > R$) and the fields penetrate uniformly the whole plasma. The absorbed power is given by:

$$P_{abs} = \frac{1}{2} \frac{n_e e^2 \pi \nu_{eff} \mu_0^2 N^2 R^4}{8ml} I_{rf}^2 \quad (2.42)$$

that is, proportional to the electron density.

$$P_{abs} \propto n_e I_{rf}^2 \quad (2.43)$$

From these two relations (2.41 and 2.43) we establish the diagram shown on figure 2.6.

At low rf current ($I_{rf} < I_{min}$), there is no possibility of inductive operation (dashed curve). In this case, the discharge operates in the capacitive mode. Increasing the current (or the power) leads to $E \rightarrow H$ transition.

2.4.3 Helicon modes (W)

Helicon power absorption have been extensively discussed above. Helicon modes are excited at high plasma density and the power absorption is resonant to the mode density. Therefore, the diagram for absorbed power as a function of the plasma density resembles a peak centered at n_0 , as shown on figure 2.7.

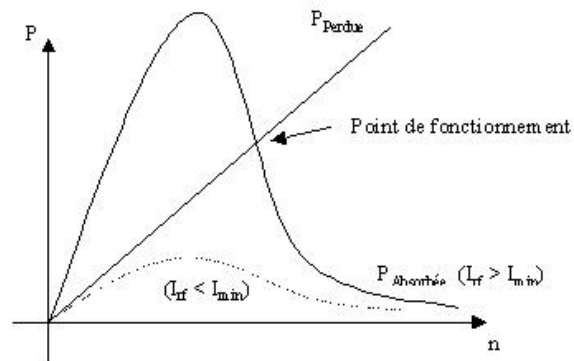


Figure 2.6: Absorbed and loss powers as a function of plasma density in the inductive mode

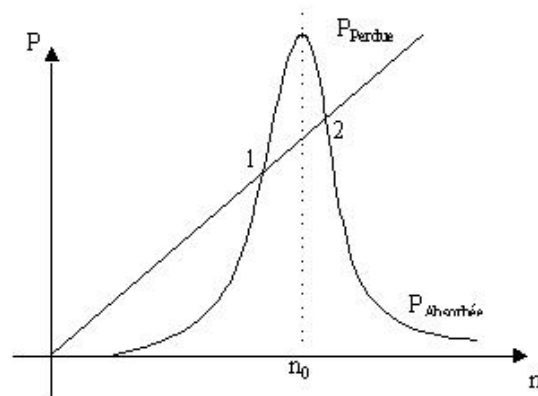


Figure 2.7: Absorbed and loss powers as a function of plasma density in a given helicon mode

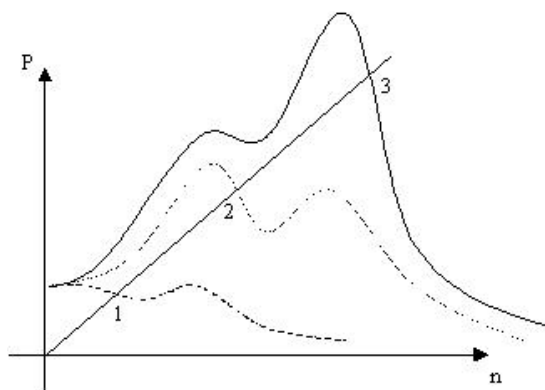


Figure 2.8: Absorbed and loss powers as a function of plasma density in a real helicon reactor, i.e. with capacitive, inductive, and helicon coupling

2.4.4 $E \rightarrow H \rightarrow W$ transitions

The "real" helicon reactor can operate in three different modes: the capacitive mode (E mode), for low power, the inductive mode (H mode), for intermediate power and finally the helicon mode (W) for high power. As the power is increased, transitions from capacitive to inductive to helicon modes are observed. Therefore, if the three modes are superposed on the same figure, the diagram for the absorbed and loss power looks like the one shown on figure 2.8.

The three possible regimes are sketched on the figure: (i) point 1 represents the operating point for capacitive coupling (dashed line), (ii) point 2 represents the operating point for inductive coupling (dot line), (iii) point 3 represents the operating point for the first mode of helicon coupling (solid line).

In reality, each coupling represents a fraction of the absorbed power. In figure 2.9 the fractional powers are shown as a function of the electron density. These results come from a global model of the helicon reactor by Boswell and Lieberman [27], in which collisionless power absorption was ignored.

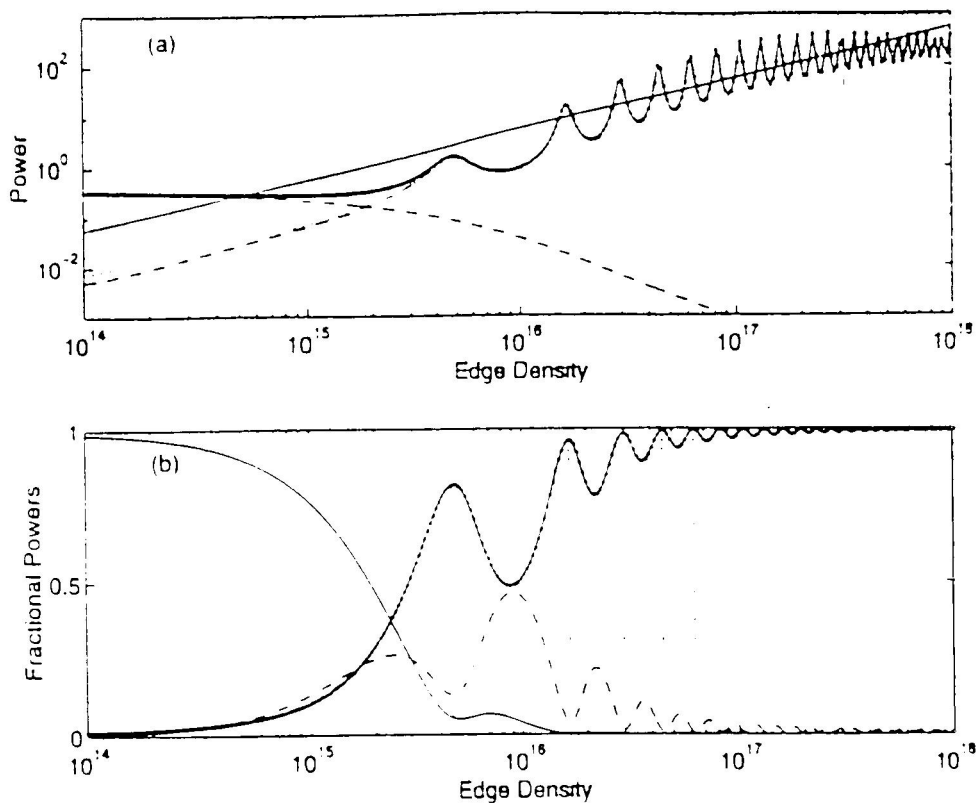


Figure 2.9: Power absorbed in each mode

Chapter 3

Double layer general theory

A current carrying plasma can sustain various non linear electrostatic structures. Among these, double layers were particularly studied. A double layer is a localized potential hump which occurs naturally in the ionosphere but which has also been reported in some laboratory experiments. The name comes from the successive layers of net positive and negative charge that are necessary to create the electrostatic step potential (cf. Fig. 3.1). A property of practical importance is that particles traversing a double layer are accelerated by the net potential difference. We give in the following a short critical reading of some of the theoretical

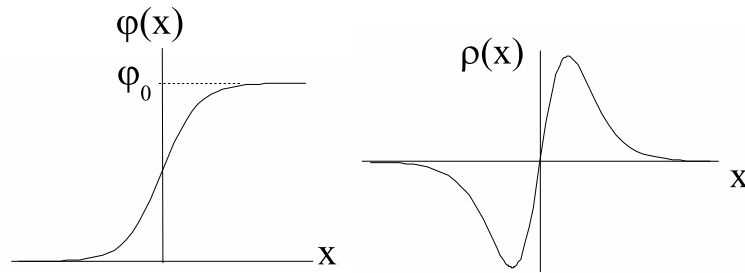


Figure 3.1: Double layer electrostatic potential (left) and the corresponding density (right).

approaches used to investigate stationary double layers.

1. The Sagdeev potential approach. A very general and appealing concept, known as the Sagdeev potential, has been introduced by Sagdeev in the context of cooperative phenomena and shock waves in collisionless plasmas [28]. As it will be shown in the following, this approach gives in a very direct way, necessary conditions for the existence of double layers in a plasma.

We focus on one dimensional multi-ion plasmas investigated within a fluid description. Poisson's equation for electrostatic potential φ reads as

$$-\epsilon_0 \frac{d^2\varphi}{dx^2} = \rho(x),$$

where ρ is the total charge density of the plasma. When it is possible to obtain the density as a functional of the potential : $\rho[\varphi]$, one can introduce the Sagdeev potential

$V[\varphi]$ which is defined by the relation

$$V[\varphi] \equiv \int^{\varphi} \rho[\psi] d\psi \quad (3.1)$$

Then, using $\rho = dV/d\varphi$, Poisson equation can be integrated once to give

$$\frac{1}{2} \epsilon_0 \left(\frac{d\varphi}{dx} \right)^2 + V[\varphi] = \Pi, \quad (3.2)$$

where Π is a constant. This can be regarded as the energy of a fictitious particle located at a "position" φ , with a "velocity" $d\varphi/dx$, where the "time" is given by x . It can be noticed that the Sagdeev potential has the same dimensionality as an energy density or a pressure.

We note φ_0 the potential across the double layer. It is normally required that both the net charge $\rho(x)$ and the electric field $E \equiv -d\varphi/dx$ must vanish at each side of the double layer. Using (3.1) and (3.2), the Sagdeev potential must satisfy the conditions

$$V'[0] = V'[\varphi_0] = 0, \quad \text{and} \quad V[0] = V[\varphi_0] = \Pi. \quad (3.3)$$

From (3.2) again, we have $\epsilon_0 E^2/2 = \Pi - V[\varphi] \geq 0$ and hence the Sagdeev potential must satisfy in addition the inequality

$$V[\varphi] \leq \Pi. \quad (3.4)$$

This equation must be fulfilled in particular at the double layer edges, where we can expand (3.4) to $\mathcal{O}(\delta\varphi^2)$ giving

$$V''[0] \leq 0 \quad \text{and} \quad V''[\varphi_0] \leq 0, \quad (3.5)$$

where we used (3.3).

(3.3) and (3.5) are the necessary conditions for the existence of double layers in a plasma. The situation is pictured on Fig. 3.2. From this picture it is clear that the potential must be very finely tuned in order that the fictitious particle starting at rest at one maximum, rolls down the potential and comes to rest at the other maximum.

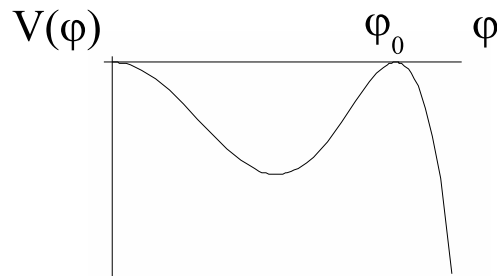


Figure 3.2: Sagdeev potential of a double layer.

Let us explain how this potential can be obtained from the equations of motion of the various components of the plasma. Inertial effects are negligible for electrons which

are in Boltzmann equilibrium with the electrostatic field. The charge density, i.e. the derivative of the electron contribution to the Sagdeev potential $V_e[\varphi]$, reads :

$$\rho_e(x) \equiv V_e'[\varphi] = -en_{e0} e^{+e\varphi/k_B T_e}, \quad (3.6)$$

where T_e is the electron temperature and n_{e0} the electron density where $\varphi = 0$. The electron contribution to the Sagdeev potential is obtained by integration :

$$V_e[\varphi] = Cte - k_B T_e n_{e0} e^{+e\varphi/k_B T_e} \quad (3.7)$$

From this expression it is clear that the electron Sagdeev potential is related the electron pressure.

Opposite to electrons, positive ions are treated in the simplest models as purely inertial particles. This approximation is relevant when the ionic temperature T_+ is negligible in comparison with the electron temperature, which is often a good approximation. In that case, the ionic density n_+ is obtained from energy conservation $m_+ v_+^2/2 + e\varphi(x) = m_+ v_{+0}^2/2$ and from the ion equation of continuity $n_+ v_+ = n_{+0} v_{+0}$. In these equations the index 0 refer to the points where the potential vanishes. The positive ionic contributions V_+ and V_+' to the Sagdeev potential are given by

$$V_+'[\varphi] \equiv \rho_+(x) = +en_{+0} \left(1 - \frac{e\varphi}{m v_{+0}^2/2}\right)^{-1/2}, \quad (3.8)$$

$$V_+[\varphi] = Cte - n_{+0} m_+ v_{+0}^2 \left(1 - \frac{e\varphi}{m_+ v_{+0}^2/2}\right)^{+1/2} \quad (3.9)$$

From this analysis, we conclude that the total Sagdeev of an electropositive plasma is given by

$$V[\varphi] = \Pi + k_B T_e n_{e0} (1 - e^{+e\varphi/k_B T_e}) + n_{+0} m_+ v_{+0}^2 \left[1 - \left(1 - \frac{e\varphi}{m_+ v_{+0}^2/2}\right)^{1/2}\right] \quad (3.10)$$

where we used the boundary conditions $V[0] = \Pi$.

A double layer can form in the plasma if, in addition, the potential satisfy the conditions (3.3) and (3.5). The two conditions $V'[0] = 0$ and $V''[0] \leq 0$ receive a simple physical interpretation. From (3.6) and (3.8), it is readily seen that

$$V'[0] = 0 \Leftrightarrow n_{e0} = n_{+0}, \quad (3.11)$$

$$V''[0] \leq 0 \Leftrightarrow v_0 \geq u_B, \quad (3.12)$$

where we introduced the Bohm velocity $u_B = (k_B T_e/m_+)^{1/2}$. The first condition corresponds obviously to the neutrality of the plasma at one edge, while the second condition is equivalent to the Bohm criteria of formation of wall sheaths.

The two conditions $V[\varphi_0] = \Pi$ and $V'[\varphi_0] = 0$ lead to the following result:

$$\frac{e\varphi_0}{k_B T_e} = 2 \ln v_0/u_B \quad (3.13)$$

It is readily found that the last condition $V''[\varphi_0] \leq 0$ can be written as

$$\frac{e\varphi_0}{k_B T_e} \leq \ln v_0/u_B \quad (3.14)$$

Since $v_0 > u_B$, it is clear that (3.13) and (3.14) are contradictory, and hence, since all the necessary conditions are not fulfilled, we conclude that a plasma with Boltzmann electrons and cold positive ions cannot sustained a double layer. In a more general approach, Verheest and Hellberg [29] have shown that double layers of whatever amplitudes cannot exist for plasma with one Boltzmann species, no matter how many cold fluid species are present. In particular, this include the case of multi-ion plasma with cold positive and negative species. It can be notice that soliton solutions for such plasmas are not excluded.

At this point, we must underline that the case of double layers with electronegative species poses a particular problem. A major difficulty is the dynamical status of the negative ions and there is still a debate to know whether confinement or inertial effects are dominant [30, 31]. In the former case, negative ions follow a Boltzmann distribution with its own equilibrium temperature T_- , while in the latter case, the dynamical behaviour of the negative ions is similar to the positive ones. Of course, this issue is crucial for the determination of the contribution of negative ions to the Sagdeev potential, and from the discussion above, we must conclude that the formation of double layers needs Boltzmann or at least not strictly cold ionic species.

The determination of the Sagdeev potential for the general case of particles with both pressure and inertial terms poses an inherent difficulty that we report now. In that case, the energy conservation $mv^2/2 + k_B T \ln n + q\varphi = Cte$ can be recasted in the form

$$\mathcal{L}(n/n_0) \equiv \frac{mv_0^2}{2} \left(\frac{1}{n^2/n_0^2} - 1 \right) + k_B T \ln n/n_0 = -q\varphi \quad (3.15)$$

where we used the ion equation of continuity $nv = n_0v_0$. From this equation, it appears that there is no one to one correspondence between density and potential, since the equation $\mathcal{L}(n/n_0) = -q\varphi$ has either no solution or two solutions. A thorough physical discussion is necessary in order to determine the correct branch. We make this point clear in the next section where we present the complementary gas-dynamic approach.

In summary, the Sagdeev approach gives a very intuitive picture of non linear structures which can be useful in some cases. It gives, at least in principle, exact necessary conditions for the existence of double layers of arbitrary amplitudes, and it is its best achievement. Nevertheless, its success relies on the possibility to define the Sagdeev potential. Since it is an inverse process, one has to check carefully the validity of such an inversion, which is often difficult in the multi-ion case. In addition, this approach obscures some of the mechanisms that lead to the existence or not of the nonlinear electrostatic structures in a plasma (see the gas-dynamic approach).

2. The gas-dynamic approach.

In a series of recent papers, McKenzie and collaborators produce a complementary approach for the study of nonlinear electrostatic structures within a plasma [32, 33].

This point of view offers a clearer insight in the limiting factors and existence conditions for double layers structures. It does so by using Bernoulli-like invariants for each species, which bring out the gas-dynamic aspects of the underlying nonlinear modes.

In this section we consider again a multi-ion plasma. For each ionic species i , we eliminate the density n_i between the particle and energy conservation, with the result

$$\mathcal{G}(v_i/v_{i0}) \equiv \frac{1}{2} (v_i^2/v_{i0}^2 - 1) - \frac{1}{\mathcal{M}_i^2} \ln v_i/v_{i0} = -\frac{q_i\varphi}{m_i v_{i0}^2} \quad (3.16)$$

where we introduced the incoming Mach number : $\mathcal{M}_i = v_{i0}/(k_B T_i/m_i)^{1/2}$, with T_i the temperature and v_{i0} the incoming velocity of the species i . This relation, which is a particular form of the Bernoulli theorem, shows that for each species there is a compensation between kinetic, pressure and potential contributions to the energy.

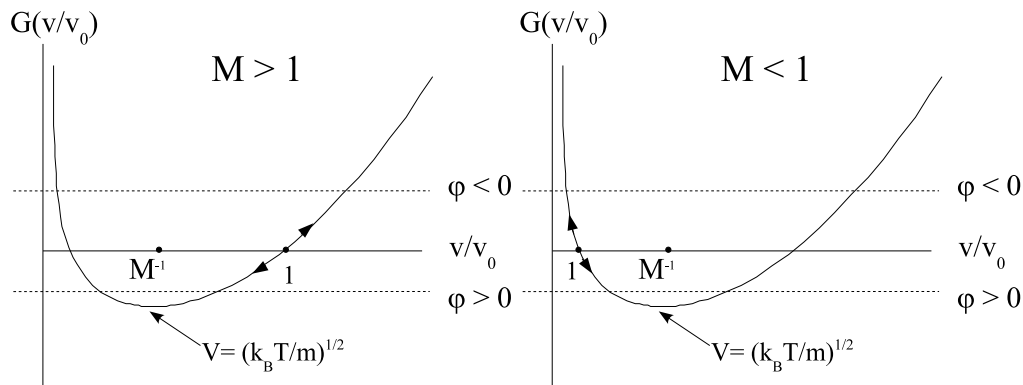


Figure 3.3: Dynamic behaviour of a positively charge particle at finite temperature when kinetic energy dominates (left), or when pressure effect dominates (right).

The function $\mathcal{G}(v_i/v_{i0})$ possesses a minimum when

$$v_i/v_{i0} = \mathcal{M}_i^{-1} \quad \Leftrightarrow \quad v_i = \left(\frac{k_B T_i}{m_i} \right)^{1/2},$$

that is when the particle reaches its own sound (or thermal) speed. Two cases must be considered in turn. If the initial velocity is such that $\mathcal{M}_i > 1$ (supersonic case), the kinetic energy dominates and, as seen on Fig. 3.3, a positive change in the potential induces a deceleration if the particle is positively charged and an acceleration if the particle is negatively charge. This is the familiar and intuitive picture and it produces an increase of the density for positively charged particles. On the other hand, if pressure effect are dominant, i.e. when the incoming flow is subsonic $\mathcal{M}_i < 1$, then exactly the opposite result follows : a positive change in the potential induces an acceleration if the ion is positively charged, and hence there is spread-out.

The consequences of this approach on the formation of a double layer in a multi-component plasma are the following. Since electrons are purely Boltzmann species, electron densities must follow the double layer potential, while ionic densities must be enhanced or depleted depending of their electric charge and initial velocities. Consequently, it is very dubious that the sum of the ionic depletions or enhancements allow the downstream charge-neutrality requirement.

One way to maintain charge neutrality at either end of the transition is to introduce trapped particles upstream or/and downstream by some process like external electromagnetic fields for example. These additional ionic populations act as pressure reservoirs which adjust the ionic densities up to charge neutrality on each side of the double layer.

3. The reductive perturbation approach.

For completeness, we want to mention another approach which has produced a huge amount of papers in the field. This approach relies on perturbation theory applied to the Sagdeev potential.

For small enough electrostatic potential φ , it is possible to expand the Sagdeev potential up to fourth order which yields in (3.2)

$$\frac{1}{2} \epsilon_0 \left(\frac{d\varphi}{dx} \right)^2 = \frac{A}{2} \varphi^2 + \frac{B}{3} \varphi^3 - \frac{C}{4} \varphi^4, \quad (3.17)$$

where the coefficients A, B, C depend of the physical parameters of the model (incoming velocities, temperature, densities ...), and where we set $\Pi = 0$. If double layers are expected, the conditions imposed on the Sagdeev potential are such that (3.17) have to be written in the form

$$\frac{1}{2} \epsilon_0 \left(\frac{d\varphi}{dx} \right)^2 = -\frac{C}{4} \varphi^2 (\varphi - \varphi_0)^2, \quad (3.18)$$

The conditions for double layers thus follows as

$$\varphi_0 = 2B/3C \quad \text{and} \quad 2B^2 + 9AC = 0, \quad (3.19)$$

with $A > 0$ and $C < 0$. It turns out that the differential equation (3.18) can be readily integrated with the expected result

$$\varphi(x) = \frac{\varphi_0}{2} (1 - \tanh(Ax^{1/2}/2)) \quad (3.20)$$

This method offers a systematic way for studying the condition of existence of double layers in various guises. It has been extensively used to investigate the role of the physical parameters and/or the number of species in the plasma. It is generally well considered, probably because of its link with some important non linear paradigms like the Korteweg-de Vries equation [34]. Nevertheless, it must be kept in mind that this perturbative approach is limited to weak amplitudes double layers. It has even been shown that the terms neglected in this approach can lead to wrong qualitative results [35, 36]

Chapter 4

HDLT: the electropositive Double Layer with diverging magnetic field

We first tried to reproduce Charles and Boswell experiment in the LPTP Helicon reactor. The system was run in pure argon at low pressure, typically 1 mTorr and below. A strong diverging magnetic field is produced by circulating a current up to 12 A in the source coils (the diffusion chamber coils being current-free). Figure 1.2 shows the amplitude of the magnetic field along the axis of the reactor; in the following text, the amplitude of the magnetic field is specified as the maximum amplitude (namely the amplitude of the field in front of the antenna breeds). Both the Langmuir probe and the RFEA have been used to characterize the plasma parameters.

Since the main difference between our system and ChiKung is the how the source tube is ended, we have investigated three different boundary conditions, specified on section 4.6. The results are extensively presented in the followings, but can be summarized as follows:

- A double layer has been measured with the RFEA at very low pressure (below 1 mT) and sufficiently high B field (above 45 G) with the three distinct boundary conditions.
- The double layer could not be measured with the Langmuir probe.

All trends emphasized by the ANU team seem to apply to our experimental data, as well as absolute numbers measured. Our results do not allow to draw conclusions on the viability of the concept. For instance, (i) we do not know if the double layer will form when the downstream region is the deep space, (ii) ion detachment from the magnetic field lines has not been studied.

4.1 Experimental evidence of Double Layer formation

To find the double layer, we first measured the plasma potential as a function of the altitude, hoping to identify a potential step. The results are shown on figure 4.1 for a low pressure argon plasma with two magnetic field amplitude. It appears that the potential has indeed two levels (the potential being higher in the source), but they seem to be joined by a smooth potential gradient rather than the expected step. On view of these results, we first conclude that the double layer was not formed before postulating that the double layer may have been perturbed when transpierced by the Langmuir probe.

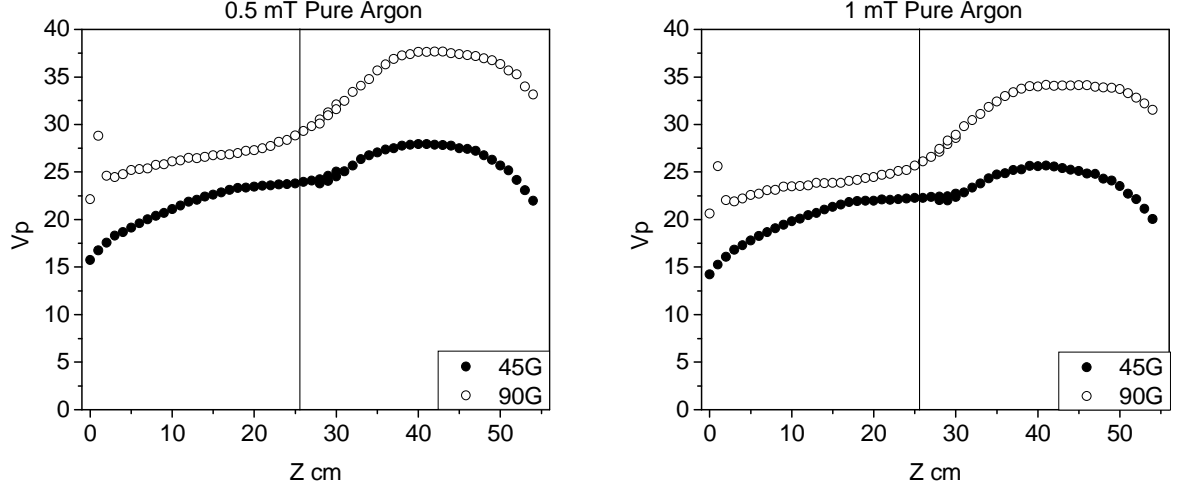


Figure 4.1: Plasma potential as a function of altitude as measured by the Langmuir probe. These curves suggest that the double layer is not formed.

The RFEA experiments were carried out to verify the previous prediction. Indeed, the double layer was formed when operating at low pressure and high B field. We have measured ion distribution functions such as the one shown on figure 4.2. The distribution presents two peaks, an evidence of the ion beam resulting of the DL formation. These peaks can be fitted by least mean square method by two gaussian peaks with the same dispersion (which is typically 6 V in the D.L. case), respectively of amplitude A_p at the plasma potential and A_b at the beam potential. The measurement corresponds to the collection of two distinct populations of ions: (i) the local ions (density n_p and average velocity $v_{Bohm} = \sqrt{\frac{kT_e}{M_+}}$) fall through the sheath of the grounded analyzer and (ii) the beam ions (density n_{beam} and average velocity v_{beam}) accelerated into a beam through the DL. Thus the two component of flux are expressed $\Gamma_{plasma} = \frac{A_p}{A_p+A_b}\Gamma_+$ and $\Gamma_{beam} = \frac{A_b}{A_p+A_b}\Gamma_+$ respectively for the local flux and the beam flux.

The local plasma density is then computed as (T being the grid transparency)

$$n_p = \frac{\Gamma_{plasma}}{qT^4v_{Bohm}} \quad (4.1)$$

Similarly, the ions accelerate through the potential drop to gain kinetic energy, leading to the following beam velocity

$$v_{beam} = \sqrt{\frac{2q(V_{beam} - V_{plasma})}{M_+}} \quad (4.2)$$

Thus, the beam density is computed as

$$n_{beam} = \frac{\Gamma_{beam}}{qT^4v_{beam}} \quad (4.3)$$

Figure 4.3 shows results obtained at 0.17 mT, 90 G, 250 W as a function of the axial position. For positions below 27 cm, the IEDF clearly shows two peaks while only one

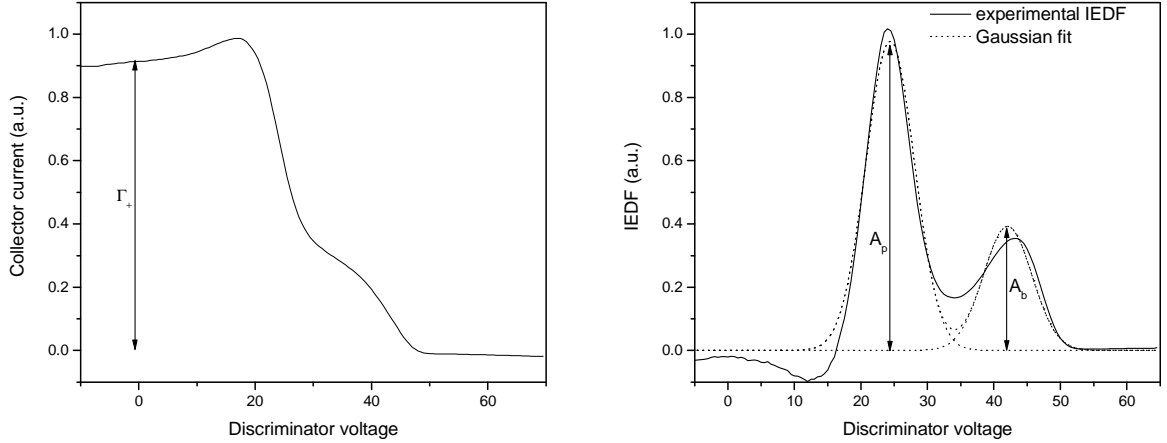


Figure 4.2: Typical acquisition signal from the RFEA. (a) Collector current as a function of Discriminator voltage for a 0.1 mT, 90 G, 250 W discharge, with the RFEA at located on the median plan of the diffusion chamber ($z = 14$ cm). (b) IEDF computed from $-\frac{dI_c}{dV_d}$ and best fit with a double gaussian having the same dispersion.

single peak is present above that altitude. The data can be analyzed as follows: the plasma potential and plasma density are roughly constant below 27 cm, with the presence of a beam at 42 V, whose amplitude is increasing exponentially when going upwards; above 27 cm, one single peak at about 42 V is obtained, with a plasma density 10 times higher than downstream, and increasing when moving up into the source tube. This strongly suggests the presence of an abrupt increase of the plasma potential at $z \approx 27$ cm, associated with a dramatic increase in the plasma density, i.e. the double layer. This double layer is associated to the presence of a beam in the low potential region, which speed is determined by the high potential region. The plasma density is determined with an electron temperature assumed to be spatially homogeneous, which was measured to be 5 ± 0.5 eV at 0.17 mT in the diffusion chamber. The voltage difference between the beam and local plasma component being 13 eV, the beam speed can be estimated by

$$v_{beam} = \sqrt{\frac{2q(V_b - V_p)}{M_+}} \approx \sqrt{5}v_{Bohm} \approx 2.2v_{Bohm} \quad (4.4)$$

The beam measured downstream of the D.L. is therefore supersonic. The higher the D.L. amplitude for a given electron temperature, the higher the specific impulse should be.

At 10 cm downstream of the double layer, the plasma beam is estimated to be 0.3 the local plasma density, which is consistent with the results obtained at the ANU.

4.2 Influence of the magnetic field strength

The presence of a sufficiently high and diverging static magnetic field is required to get a double layer. We show on figure 4.4 a parametric study of the formation and behaviour of the double layer as a function of the magnetic field strength. These results were obtained with the RFEA at $z = 20$ cm, at a pressure of 0.17 mT, and a power of 250 W. For B field below

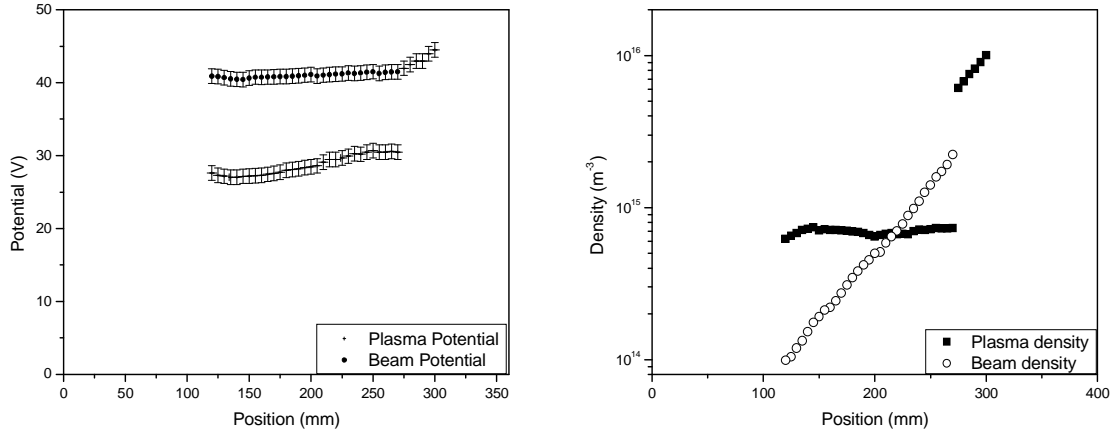


Figure 4.3: Evidence of double layer existence in pure argon at 0.17 mT, 90 G, 250 W: (a) local plasma potential and beam potential as a function of axial position, (b) plasma density and ratio of beam flux to local flux as a function of axial position.

45 G, the IEDF shows only one peak, with a density being fairly high ($10^{16}m^{-3}$). Above 45 G, the IEDF shows an evidence that a double layer exists. While the plasma density is slightly decreasing with increasing B field (from $3 \cdot 10^{15}m^{-3}$ at 45 G to $1 \cdot 10^{15}m^{-3}$ at 90 G), the plasma potential is slightly increasing from 28 V at 45 G to 30 V at 180 G. But the main characteristic is that the double layer amplitude (around 15 V for these conditions) increases very slowly for B field above 45 G. The beam density is only slightly fluctuating and seems to follow the local plasma density behaviour. However it is difficult to compare beam densities for different operating conditions since the position of the D.L. and the upstream density could vary (refer to subsection 4.7 for some comments on the experimental limitations).

These results are consistent with those obtained at the ANU and some conclusions could be given as for propulsion requirement at a given power: the double layer amplitude seems to be independent of the B field above a critical value, thus limiting the amount of dc current required to generate the moderate B field (namely 45 G in our system). Although the DL amplitude is independent of the magnetic field magnitude it may depend on the gradient strength.

4.3 Influence of the gas pressure

The double layer only appears at sufficiently low operating pressure. We show on Figure 4.5 the influence of the pressure on the D.L. characteristics for a 90 G magnetic field and a operating power of 250 W for a RFEA positioned at $z = 20$ cm. At gas pressures above 3 mT only one peak is measured and no D.L. is present. Below 1 mT, two peaks can be determined, thus giving evidence of a D.L. When decreasing the pressure the plasma potential downstream of the D.L. remains constant, while the upstream potential increases. Thus the D.L. potential increases drastically with decreasing pressure. The beam flux is also increasing with decreasing pressure; which is consistent due to the increase in acceleration from the D.L. potential and decrease in collision frequency. The plasma density is scaling as expected:

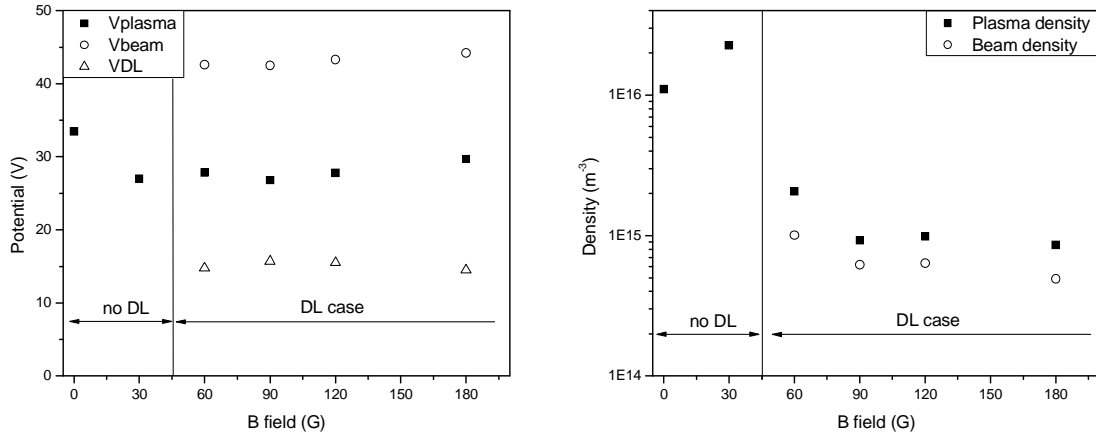


Figure 4.4: Influence of the static magnetic field amplitude at 0.17 mT, 250W. The RFEA is located at $z = 20$ cm. (a) local plasma potential and beam potential as a function of magnetic field strength, (b) plasma density and beam density as a function of magnetic field strength.

decreasing with decreasing pressure, since the electron temperature required to sustain the discharge is increasing. No discharge could be sustained below 0.08 mT. However, below 0.10 mT, the measured IEDFs show only one peak. Thus only a small window in pressure could lead to the formation of a D.L. This feature was also clearly evidenced at the ANU. For propulsion requirements, the highest specific impulse is obtained at the lowest pressure, but on the other hand the thrust may not be kept constant since the density is decreasing with decreasing pressure.

Once again these trends have already been published by the ANU group. A slight discrepancy in terms of absolute values (DL amplitude, pressure window etc.) arises between the ANU data and ours. However, these are fairly small and could be explained by the fact that we measure the pressure with a gauge that is designed to run in the range 0-100 mT. Therefore, our measured pressure below 0.5 mT could easily have absolute errors of about 50%.

4.4 Influence of the rf power

For near earth planet exploration, the scaling up to high power is very important. We therefore experimentally investigated the influence of the rf power at given pressure and magnetic fields. The experimental results have been acquired at 0.2 mT and a magnetic field of 90 G. When increasing the power, the plasma potential keeps on decreasing, while the plasma density increases quasi linearly. The power coupling to the plasma might drastically change from 250 W (capacitive or inductive coupling) to a few thousands W (wave mode coupling), thus the decrease in plasma potential is to be unexpected. The plasma density is also known to scale proportionally to the power.

One important result is that the D.L. amplitude remains constant (less than 5% fluctuations) from 150 W to 1000 W, which is an important result for propulsion requirements. On

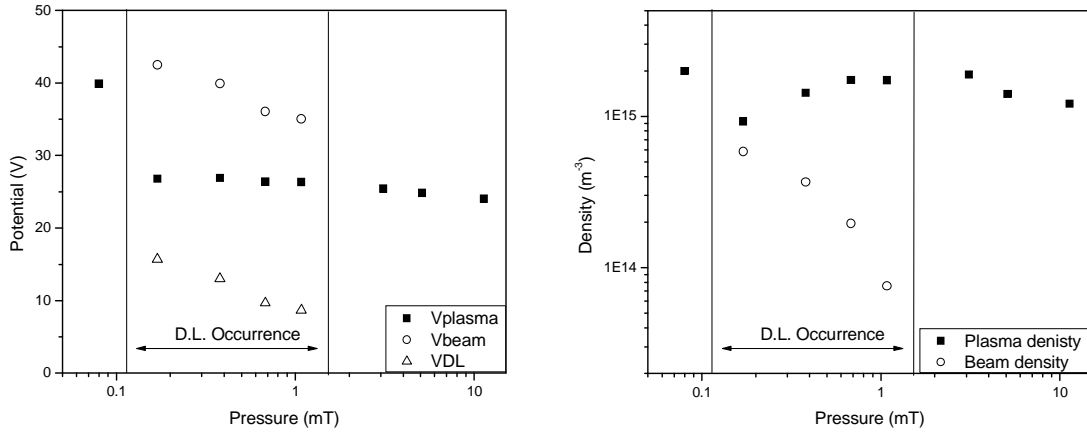


Figure 4.5: Influence of the pressure at 250W for a 90 G magnetic field. The RFEA is located at $z = 20$ cm; (a) local plasma potential and beam potential as a function of magnetic field strength, (b) plasma density and beam density as a function of operating pressure.

the other hand it appears that the beam density is not increasing at the same rate as the local plasma density. However, due to the experimental set up limitations one cannot give any definitive conclusion for propulsion (refer to subsection 4.7 for some comments on the experimental limitations).

4.5 Ignition of the electropositive double layer

We set up a time resolved acquisition system that allowed us to measure the ignition and the time development of the D.L. To get some insight into the DL formation, the discharge was operated pulsed, with a $750 \mu\text{s}$ on period and $500 \mu\text{s}$ off period that allows the plasma to extinct between pulses. The RFEA's discriminator voltage biased is kept constant during 256 pulses and increased step by step afterward. The collector current is acquired on a large memory scope, averaging over 256 periods to reduce noise measurements (the temporal behaviour has been checked to be reproducible between each pulse). The data are then computer-based processed to obtain time-resolved IEDFs. These are show on figure 4.7. These data are processed to follow the amplitude and potential of the two bumps, and are given on figure 4.8. The beginning of the 'on' time is located at $t=20 \mu\text{s}$, and only one bump is present before $t=50 \mu\text{s}$. Then the beam potential is quickly set (over $10\text{-}20 \mu\text{s}$), while the downstream plasma potential keeps on decreasing (from 38 to 30 V) over the next $50 \mu\text{s}$. The amplitudes of both the beam component and local plasma component are increasing and saturates after $150 \mu\text{s}$ of operation, with the same time scale for both peaks.

4.6 Influence of the boundary conditions

We have investigated the influence of changing one of the boundary condition of the source tube, namely how the source tube is ended. It appears that the position of the glass tube in ChiKung experiment plays an important role in the beam amplitude [4]. Our system is

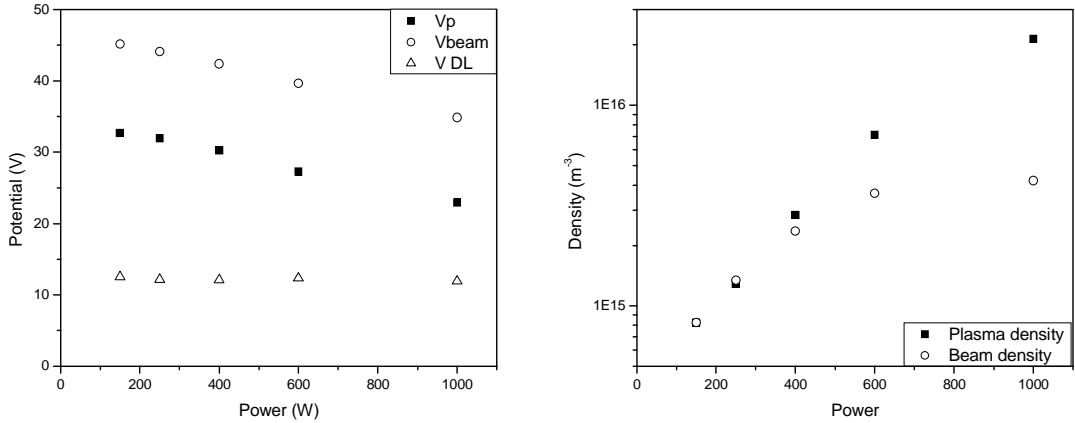


Figure 4.6: Influence of the power at 0.2 mT for a 90 G magnetic field. The RFEA is located at $z = 23$ cm. (a) local plasma potential and beam potential as a function of axial position, (b) plasma density and ratio of beam flux to local flux as a function of axial position.

operated with the pumping system set at the end of the source tube, thus the tube needs to be ended by a grid. However three different configurations have been experimentally studied. These are described on figure 4.9. All results presented above and in section 5 were with the condition (a), namely a insulating grid with a piece of grounded metal at the end of the pyrex tube.

Figure 4.10 show direct RFEA measurements and processed IEDF normalized to one at the plasma potential, when the RFEA is placed at $z = 20$ cm, for a 0.17 mT, 90 G, 250 W plasma. The ion saturation flux is the same within less than 3%; and the peaks amplitudes are decreasing by a few percent (8% from geometry (a) to geometry (c)). A noticeable variation of the potentials is observed: The local plasma potential is decreasing: 26.5 V, 25.5 V and 24.5 V, while the beam potential is increasing: 42.5 V, 44.2 V, 46.5 V, for geometry (a), (b) and (c) respectively. However the broadening of the peaks slightly increases when scanning from geometry (a) to geometry (c) for unexplained reasons. These results are significantly different from those published in [4] which showed that the beam component relative to the plasma component could triple when changing the position of the end plate by only 2 cm.

Interestingly, the double layer was found for all boundary conditions, including the dc connected (condition a) case. We therefore conclude that the DL is not necessarily current free. All experiments conducted show that the same trends are kept in term of pressure, B field, position whatever the source boundary conditions. However, as shown in figure 4.10, the DL amplitude changed noticeably with the boundary conditions, the higher DL amplitude being obtained for the floating conducting grid: the D.L. amplitude increases from 16 V (condition a) to 22 V (condition c) while all other experimental parameters are kept constant.

4.7 Limitations of the experimental set-up for propulsion testing

We were able to reproduce most of the results obtained at the ANU, in a reactor similar in size and conception. However we did emphasize that the boundary conditions are not so restrictive since a beam was observed whatever terminates the plasma. The window of D.L. occurrence can be summarized as follows:

- Low operating pressure (between 0.1 and 1 mT) with a maximum in D.L. potential, thus acceleration, at the lowest pressure
- Diverging B field of sufficiently high amplitude (above ≈ 45 G).

However our experimental set up is not appropriate to address a few of the most fundamental question arising when aiming at propulsion. One can summarize a few of them

- Limited pumping efficiency. Our system has finite volume and pumping speed, thus the plasma, created in the source, is diffusing in the diffusion chamber across the D.L. and fills the diffusion chamber. It is not possible to get a D.L. without a secondary plasma of relatively high density (10^{15}m^{-3} connected to the diffusion chamber walls. If used as a thruster, the pressure downstream of the D.L. would be nearly zero, and possibly no plasma could be sustain outside the thruster. Would a D.L. still form and would it keep the same characteristics and trends? One way to experimentally investigate this important issue would be to test a HDLT in a big vacuum facility test to be able to simulate space environment.

The equilibrium reached by the plasma involves the downstream plasma in such a way to ensure total ion flux continuity. The continuity between the downstream ion flux Γ_{+d} and the upstream flux Γ_{+u} can be written at the D.L. position:

$$\Gamma_{+d} = n_{+d}v_{bohm} + n_{beam}v_{beam} = n_{+u}v_{bohm} = \Gamma_{+u} \quad (4.5)$$

From this we can see that both n_{beam} and v_{beam} (and the D.L. amplitude since $v_{beam} = \sqrt{\frac{2qV_{DL}}{M_+}}$) depends on the ratio between n_{+d} and n_{+u} .

Thus all experimental results presented above are strongly dependent on the presence of the downstream plasma: D.L. amplitude, beam density and beam speed. These results could be drastically changed if the HDLT was operated in space.

- Particle detachment. Since the HDLT concept requires a highly diverging magnetic field of large amplitude, the motion of charged particles is helical. The magnetized particles follow the magnetic field lines, with a motion in the perpendicular direction to the magnetic field limited by the local Larmor radius. The question that arises is: do the particles detach from the closed magnetic field lines (i.e. if the particles free themselves from the magnetic field of the source), and if yes how. The expanding magnetic field created by the solenoids influences the shape of the ion beam as it expands into space, giving the beam divergence and thereby affecting the net thrust generated by the beam. In the extreme case, where the magnetic-field intensity is high enough,

the charged particles exiting the nozzle will be attached to the closed magnetic-field lines and no net thrust will be provided. At the other extreme, the beam velocity field will be determined mainly by the parallel acceleration across the double layer and will have almost no divergence, so thrust will be generated at maximum efficiency. A model has been developed by the Australian team [37] in which the actual particle motion is solved by computer simulation in the presence of the diverging magnetic field. It appears that the ions will detach from the magnetic field and that the divergence is low (a few degrees), thus confirming the experimental measurement of beam divergence in the ChiKung reactor [5].

However, this model includes only the positive ions and the ambipolar field was ignored. The energy discrepancy between massive ions and light electrons is such that the Larmor radii of positively and negatively charged species are of different scales; thus the electrons should follow the magnetic field lines since their Larmor radius is less than a mm. The antagonist behaviour of the particles will lead to an ambipolar electric field that could increase the divergence of the beam and thus decrease the thrust.

The experimental analysis of beam divergence has been done in a small experiment, whose walls are conducting in the downstream region. This boundary condition could change drastically the particle motion. In the experimental setup the electro-neutrality requires equal ion and electron fluxes integrated over the entire wall surface. Because of the conducting walls in the diffusion chamber, currents may flow in the wall and the local flux balance can be violated. In space-like conditions, the local flux balance would be required. Once again, to fully test the thrust efficiency of the device, a measurement of the beam divergence (and therefore of particle detachment) should be processed in a big vacuum facility.

- Thrust measurement. The thrust and specific impulse can only be estimated from our and published results. To get a precise idea of how space-like conditions and particle detachment would act on the D.L., a direct measurement needs to be done in a vacuum facility equipped with micro balances. However an estimate of the thrust efficiency is given in the last section.

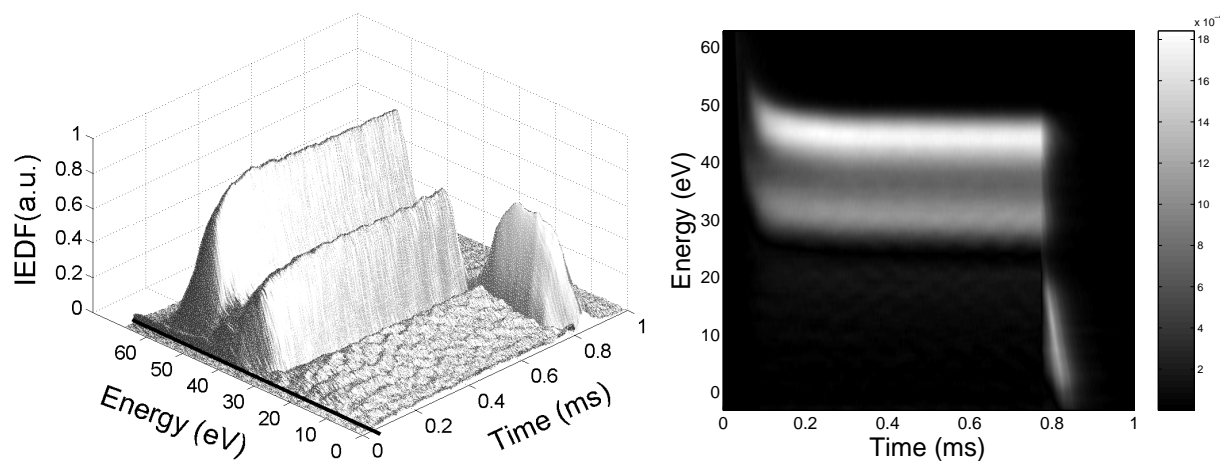


Figure 4.7: Time resolved IEDF during pulsed operation of the discharge at 0.2mT, 90 G, 250 W. The RFEA is at $z = 20$ cm. (a) 3d mapping of the IEDF, (b) gray level image.

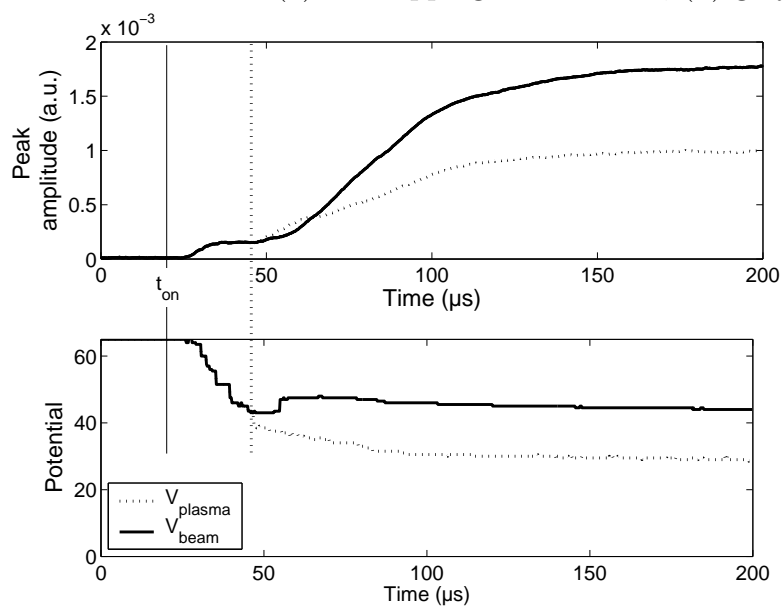


Figure 4.8: Time development of the IEDF peaks during pulsed operation of the discharge at 0.2mT, 90 G, 250 W. The RFEA is at $z = 20$ cm.

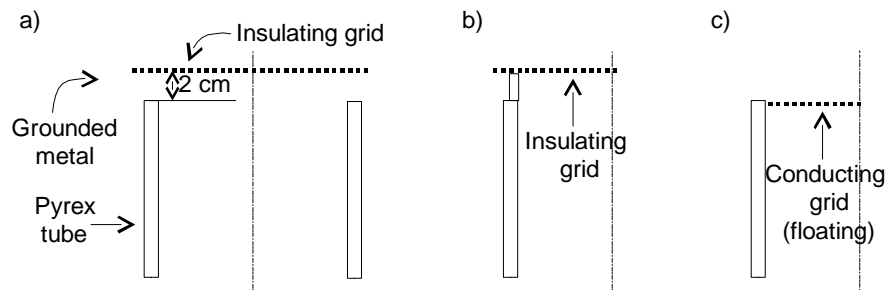


Figure 4.9: Source tube ends. Three boundary condition have been investigated: (a) an insulating grid terminates the plasma, with about 2 cm of grounded metal between the pyrex tube and the grid, (b) same as (a) with a pyrex tube inserted to shield the grounded metal parts from the plasma, (c) a conducting floating grid terminates the plasma at the end of the pyrex tube

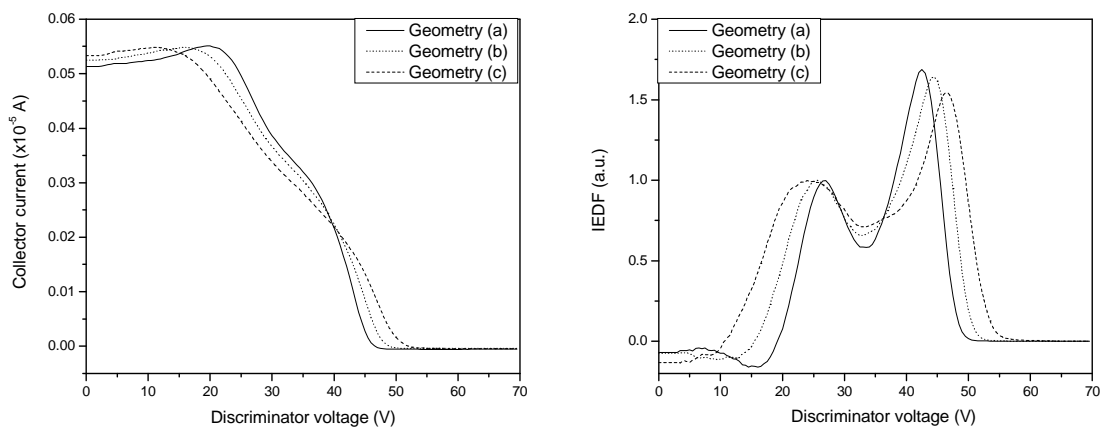


Figure 4.10: Influence of the boundary conditions on the measured IEDFs. Direct measurements from the RFEA and computed IEDFs for discharge operating conditions 0.17 mT, 250 W and a magnetic field of 90G. The three geometries are defined on figure 4.9.

Chapter 5

The Electronegative Double Layer Concept

For the results presented in the following, the magnetic field has been turned off. An electronegative gas has been added to argon in order to check the possible formation of a Bfield-free double layer. The results presented here detail the results published in [38] and [39].

5.1 Stable double layers

5.1.1 Experimental evidence of a double layer potential structure with Langmuir probes

The figure 5.1a shows the axial evolution of the plasma potential and the electronegativity for a SF₆ concentration of 6%. The gas pressure was 1 mTorr and the input power was 600W. The dashed line represents the position of the interface between the source and the diffusion chamber. The plasma potential decreases continuously from the source to the diffusion chamber, as expected for an expanding plasma which exhibits a gradient in the electron density, while the electronegativity remains roughly constant along the axis. There is evidently no DL. For these pressure and power, the transition toward the formation of the DL is observed to occur at about 8% SF₆ concentration. No DL's were observed in pure argon or for SF₆ concentration below 8%. Above this concentration, the plasma potential and particles gradients are drastically changed as shown in figure 5.1b. The plasma potential presents a sharp drop at around $z = 22\text{cm}$, that is about 4 cm below the interface between the two chambers. The potential difference between the source chamber and the diffusion chamber seems to be at least 10V, although the sharp drop seems to be around 5V and located at 22cm. This sharp drop is preceded by a strong but smoother gradient that resembles a pre-sheath.

The electronegativity is also profoundly affected. It presents a sharp maximum at the DL position, with a slow decay downstream (below the DL in the diffusion chamber) and a much faster decay upstream. The variations of α are directly related to the change in the electron density, as shown on figure 5.2a. The electron density is strongly affected by the sudden drop in potential, whereas both the positive and negative ion densities seem to decrease continuously from the source to the diffusion chamber. The electron tempera-

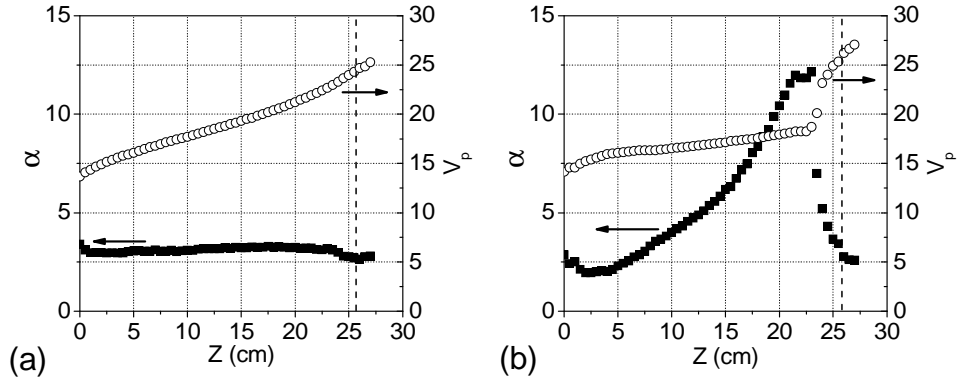


Figure 5.1: Double formation due to negative ions at 1 mTorr, 600W, without a static magnetic field. (a) 6% SF₆ added to Argon, (b) 9% SF₆ added to Argon.

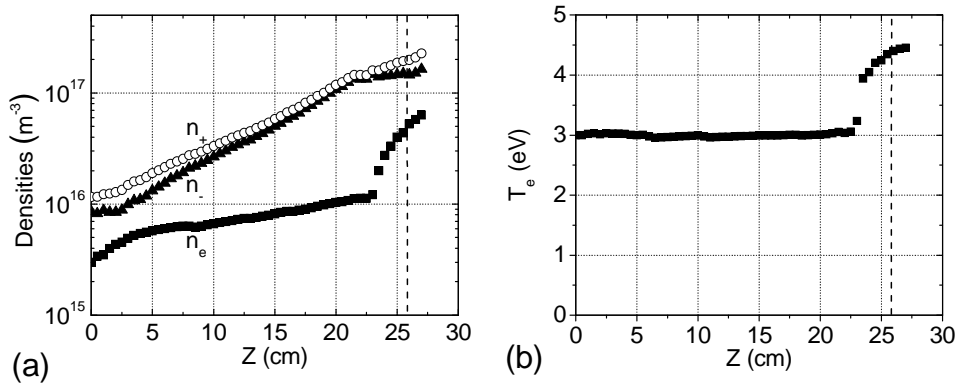


Figure 5.2: Particle densities and electron temperature associated to the Double Layer occurrence

ture changes significantly when crossing the DL. The DL acts as an internal boundary (or sheath), which separates two plasmas; a high electron density, high electron temperature, low electronegativity plasma upstream, a low electron density, low electron temperature, high electronegativity plasma downstream.

As the SF₆ concentration is increased, the location of the DL moves downward (for a 11% SF₆ mixture, the altitude is $z = 18\text{cm}$, that is 8 cm below the source exit) and the plasma potential drop becomes less abrupt, gradually replaced by a larger region of strong gradient of potential upstream, before entering the DL itself. The downstream plasma potential remains mostly constant at about 15 V. Before going to that matter, let us further discuss the stable case and note that the electrons are not far from Boltzmann equilibrium. Figure 5.3 (a) gives $\ln(n_e)$ as a function of V_p and confirms the Boltzmann hypothesis, with two electron temperatures: 3.2 eV downstream of the D.L and 4.5 eV upstream of the D.L. However the two straight lines do not cross each other at $V_p \approx 21\text{V}$, and in (b) we have the best fit of n_e following Boltzmann equilibrium if we set n_e to be $n_{e0} \exp(V_p/3)$ downstream

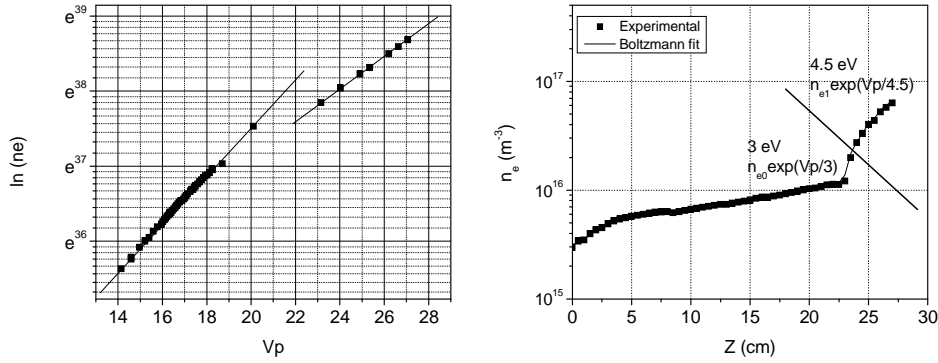


Figure 5.3: (a) Electron temperature derived from Boltzmann's law, (b) experimental densities and theoretical Boltzmann fit.

and $n_{e1} \exp(V_p/3)$ upstream with $n_{e0} = 2.7 \cdot 10^{13}$, $n_{e1} = 1.5 \cdot 10^{14}$. This may be due to trapped species in the source chamber. As we shall discuss below, the DL's become unstable for higher electronegative gas mixture. Before going to that matter, let us further discuss the stable case and note that the electrons are not far from Boltzmann equilibrium, as indicated by the dashed line in figure 5.2a, which is the theoretical electron density curve constructed from our potential and electron temperature data ($n_e = n_{e0} \exp(V_p/T_e)$, where n_{e0} was adjusted for the best fit). On the contrary, negative ions are far from Boltzmann equilibrium, and are present both sides of the DL. Since they cannot cross it from upstream to downstream (their temperature is much too small), they must be created downstream, i.e. the attachment rate must be strong in this region. This may be due to the relatively low electron temperature, and also to higher neutral gas density because of colder neutral gas (inductive discharges are known to produce significant gas heating near the coil). The negative ions created in the big buffer region downstream the DL would then be accelerated toward the source through the DL. Unlike the attachment, the ionization is probably mainly located in the source region where the electron temperature is high. Hence, positive ions are mainly produced in the source region and are accelerated downstream through the DL. The DL is therefore crossed by two ion streams in opposite directions.

The origin of the DL formation remains unclear. From our data and from visual observation, we can postulate that the DL has a spherical shape and that it is formed at the boundary between the source and the diffusion chamber, as proposed in earlier work for electropositive gases [40]. However, this geometric feature is not sufficient to explain our observations since we did not observe the DL in pure argon. We can postulate that the SF_6 addition has two main effects that contribute to the DL formation. First, the positive ions will more easily reach the ion sound limitation (a necessary condition to form a DL) since it is well known that the ion sound speed is lower in electronegative plasmas. Second, the attachment process is a very efficient loss term for electrons during the plasma expansion, which makes steeper n_e gradients and therefore higher potential gradients. This effect may be compared to the strongly divergent magnetic field used by Charles and co-workers [1], which also acts as a loss process for electrons during the expansion.

To conclude this section, we note that the DL was also formed when adding the static magnetic field (keeping the fraction of SF_6 added), without dramatic change in the DL

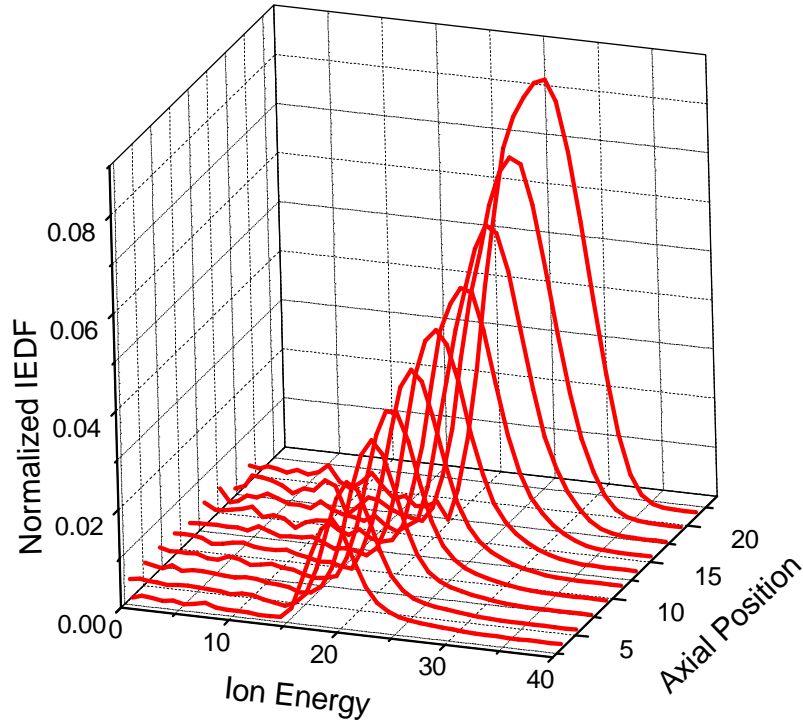


Figure 5.4: Spatially resolved Ion Energy Distribution Function in pure Ar, 1 mT, 600 W along the axis.

properties (e.g. the DL amplitude remained mostly unchanged).

5.1.2 Beam measurement in the downstream region

We were able to measure the Ion Energy Distribution Function (IEDF) using the RFEA in the presence of the electronegative double layer. The mean free path for charge exchange is proportional to $1/P$, with P the total neutral gas pressure and is 3 cm at 1 mTorr. Since the RFEA holding structure is not infinitely small compared to the vessel size, it is not possible to measure IEDFs at positions closer than 3 to 5 cm to the D.L. Thus measurements are only possible at low pressure (around 1 mTorr). The experimental data are fitted by either a single gaussian function, either a two gaussian functions when two bumps are present. The plasma potential and beam potential are then deduced from the position of the maxima of each gaussian.

Spatially resolved IEDF sequences are shown on fig 5.4 and 5.5. Figure 5.4 shows the IEDFs as a function of the position on axis for a pure argon plasma at 1 mTorr, 600W. Each IEDF shows only one peak at the plasma potential (we note that the plasma potential measured by means of RFEA are in agreement with the one processed from the Langmuir probe, with a systematic error being 1 V).

Figure 5.5 shows IEDFs for an Ar:SF₆ mixture with the same conditions as figure 5.1. The IEDF is not symmetrical, having a high energy tail due to the ion beam caused by the double layer. The presence of a beam is clearly shown for positions below 16 cm, with a

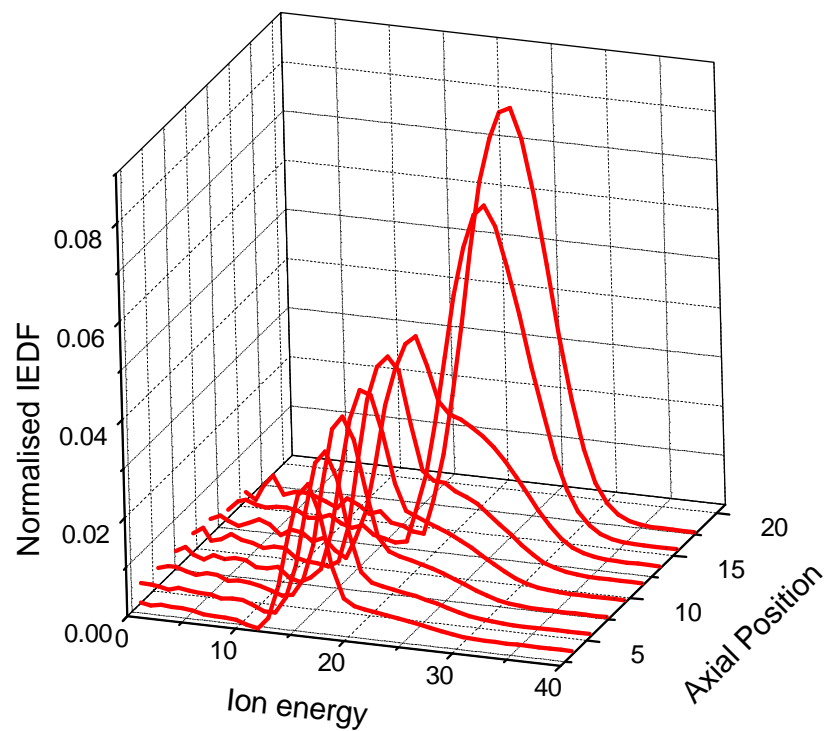


Figure 5.5: Spatially resolved Ion Energy Distribution Function in a 10% SF₆ mixture in Ar, 1 mT, 600 W along the axis. Experimental evidence of a positive ion beam is shown from the second bump in IEDFs for positions below 16 cm.

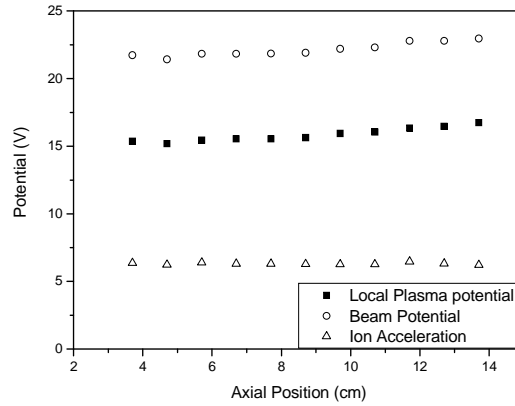


Figure 5.6: Evolution of: plasma potential, beam potential and DL amplitude as a function of position along the axis for a 10% SF_6 mixture at 1 mT, 600W.

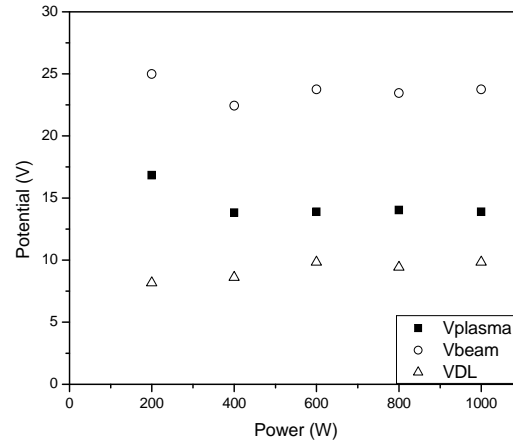


Figure 5.7: Evolution of: plasma potential, beam potential and DL amplitude as a function of Power 10% SF_6 mixture at 1 mT, at $z = 14$ cm.

decreasing amplitude when going downward. The discrepancy in D.L. position between the L.P. probing ($z \approx 21$ cm) and the RFEA probing ($z \approx 16$ cm) is due to the fact that when the distance between the RFEA and the D.L. is less than 5 cm, the RFEA attracts and destroys the DL.

The ion beam potential remains constant when going further from the D.L. as shown on Fig 5.6. We can conclude that the double layer amplitude is between 6 and 7 V and remains fairly constant when positioning the RFEA at $z = 14$ cm and varying the power, as shown on fig 5.7, and the pressure, as shown on fig 5.8.

5.2 Transition toward unstable operation

As the SF_6 concentration is further increased, the discharge becomes unstable, entering a downstream instability regime. Using a time-resolved LP system we were able to measure

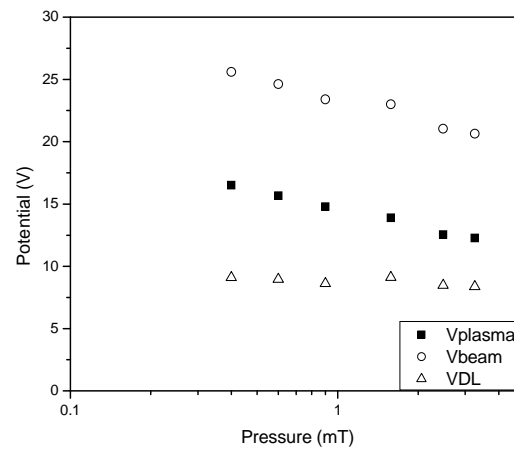


Figure 5.8: Evolution of: plasma potential, beam potential and DL amplitude as a function of Pressure 10% SF_6 mixture, at 600 W, and $z = 14$ cm.

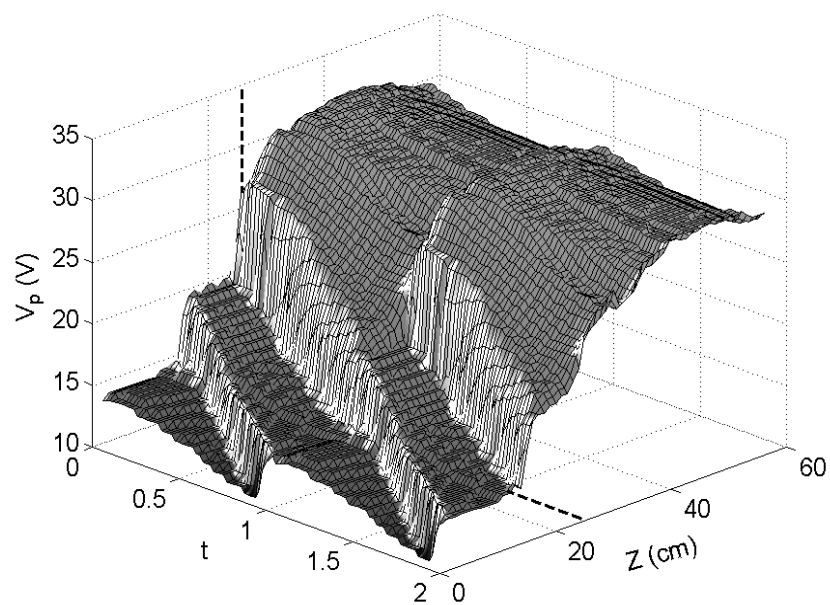


Figure 5.9: 3D mapping of the plasma potential, showing the propagation of the unstable double layer for a 25 % SF_6 mixture at 1 mT, 600W.

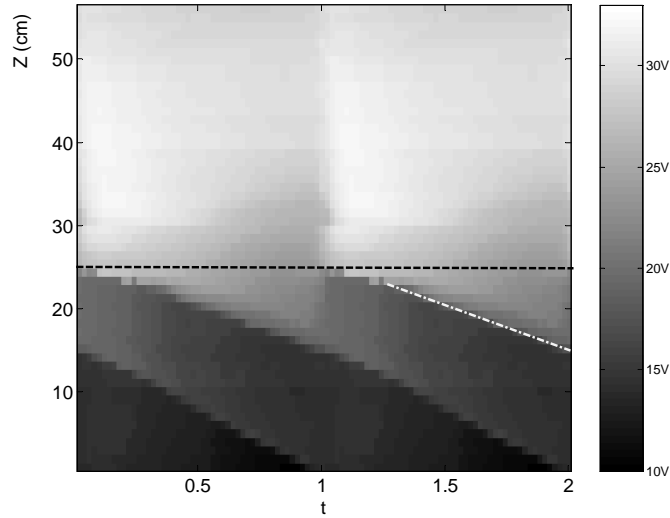


Figure 5.10: Gray-scale image of the plasma potential, showing the propagation of the unstable double layer. Some conditions as above

the temporal evolution of the plasma parameter spatial profiles. Figure 5.9 show the plasma potential measured on the reactor axis as a function of z , and as a function of time. The x-axis is the time, normalized to the instability period, and the y-axis is the position (the diffusion chamber bottom is at $z = 0$ cm). The interface between the source and diffusion chambers is at $z = 26$ cm and is shown by a black dotted line. It seems that the double layer is born at the interface between the two chambers, as it was proposed for electropositive gases [40], and moves downward as time evolves. The double-layer formation frequency and the propagation speed are such that the first double layer has not reached the bottom of the diffusion chamber when a new double layer forms upstream. Consequently, at a given time during the instability cycle, there are two potential drops in the diffusion chamber. The propagation speed is small, about 250 m/s, and mostly constant although the double layer seems to slightly speed up at the end of its travel, when the new double layer is formed. The plasma parameters are only slightly modulated in the source region, thus, it does not seem that the instability is driven by the source.

5.3 Theory

5.3.1 Model assumptions

We consider that a double layer, having a spherical shape with a radius $R_1 = 6.5$ cm, exists at the interface between the source and the expanding chamber (actually a half-sphere). The rf power is deposited in the source plasma, upstream the double layer, which will be modeled as a weakly electronegative cylindrical plasma (see the work by Lichtenberg and co-workers). The positive ion flux exiting the source is an input parameter of the downstream region model developed below (coupling between the two models). The downstream plasma equilibrium

is deeply influenced by the source plasma, however, the opposite is not true. That is the upstream plasma is only weakly perturbed by the negative particle fluxes coming from the downstream region.

The model detailed in the following describes the expanding region downstream the double layer. We consider that the expanding chamber has a spherical geometry (rather than the real cylindrical geometry) and is terminated at $R_2 \approx 4.5R_1$. In this way, the theoretical and experimental area ratios, $A(r = R_2)/A(r = R_1)$, are similar. The momentum and the conservation equations are solved for three coupled fluids in spherical (1D) geometry. The three fluids are electrons, positive ions and negative ions. The electrons are Boltzmann and we consider quasi-neutrality, $n_e + n_- = n_+$. The electron and ion temperatures are parameters, estimated from experimental results. We define the following quantities:

$$\begin{aligned}\Gamma_{\pm} &\equiv n_{\pm}u_{\pm} \\ D_{\pm} &\equiv kT_{\pm}/m_{\pm}\nu_{\pm} \\ \gamma_{\pm} &\equiv T_e/T_{\pm}\end{aligned}$$

where n_{\pm} and u_{\pm} are the ion densities and ion fluid velocities respectively, T_e is the electron temperature, T_{\pm} are the ion temperatures, m_{\pm} are the ion masses, D_{\pm} are the ion diffusion coefficients, and ν_{\pm} are the ion-neutral collision frequencies.

Particle and momentum conservation

The ion conservation equations in steady state (and in spherical geometry) are:

$$r^{-2} (r^2\Gamma_{\pm})' = Q_{\pm} \quad (5.1)$$

$$Q_+ = \nu_i n_e - K_r n_+ n_- \quad (5.2)$$

$$Q_- = \nu_a n_e - K_r n_+ n_- \quad (5.3)$$

where ν_i , ν_a and K_r are respectively the ionization frequency, the attachment frequency, and the recombination coefficient. The momentum conservation equations in steady state are:

$$\begin{aligned}\Gamma_{\pm} &= D_{\pm} \left[\pm \frac{qE}{kT_{\pm}} n_{\pm} - n'_{\pm} \right], \\ kT_e n'_e &= -en_e E,\end{aligned}$$

where E is the electric field. Using quasi neutrality and our definitions, these equations may be written in the form

$$(n_+ - n_-)\Gamma_{\pm} = -D_{\pm} ((n_+ - n_-)n'_{\pm} \pm \gamma_{\pm} n_{\pm} (n_+ - n_-)') \quad (5.4)$$

Basic equations

Equation (5.4) may be written

$$\begin{pmatrix} -D_+ \gamma_+ n_+ - D_+ (n_+ - n_-) & D_+ \gamma_+ n_+ \\ D_- \gamma_- n_- & -D_- (n_+ - n_-) - D_- \gamma_- n_- \end{pmatrix} \begin{pmatrix} n'_+ \\ n'_- \end{pmatrix} = \begin{pmatrix} (n_+ - n_-)\Gamma_+ \\ (n_+ - n_-)\Gamma_- \end{pmatrix}$$

which is equivalent to

$$\begin{pmatrix} n'_+ \\ n'_- \end{pmatrix} = \frac{\begin{pmatrix} -D_-(n_+ - n_-) - D_-\gamma_-n_- & -D_+\gamma_+n_+ \\ -D_-\gamma_-n_- & -D_+\gamma_+n_+ - D_+(n_+ - n_-) \end{pmatrix}}{D_-D_+[(1 + \gamma_+)n_+ - (1 - \gamma_-)n_-]} \begin{pmatrix} \Gamma_+ \\ \Gamma_- \end{pmatrix}$$

We finally obtain the following system of four ordinary differential equations of first order, to be solved numerically:

$$\begin{aligned} n'_+ &= \frac{D_- [\gamma_-n_- - (n_+ - n_-)] \Gamma_+ + D_+\gamma_+n_+ \Gamma_-}{D_-D_+ [(1 - \gamma_-)n_- - (1 + \gamma_+)n_+]}, \\ n'_- &= \frac{D_-\gamma_-n_- \Gamma_+ + D_+ [\gamma_+n_+ + (n_+ - n_-)] \Gamma_-}{D_-D_+ [(1 - \gamma_-)n_- - (1 + \gamma_+)n_+]}, \\ \Gamma'_+ &= \nu_i(n_+ - n_-) - K_r n_+ n_- - \frac{2\Gamma_+}{r}, \\ \Gamma'_- &= \nu_a(n_+ - n_-) - K_r n_+ n_- - \frac{2\Gamma_-}{r} \end{aligned}$$

Theses equations are normalized to facilitate numerical integration.

5.3.2 Boundary conditions

In order to solve the model one needs to define the appropriate boundary conditions. We use the following:

$$\begin{aligned} \Gamma_+(r = R_1) &= \Gamma_0 \\ \Gamma_-(r = R_2) &= 0 \\ u_-(r = R_1) &= u_B/\sqrt{\gamma_-} \\ u_+(r = R_2) &= u_B/\sqrt{\gamma_-} \end{aligned}$$

The first condition comes from the fact that most of the positive ions in the expanding region actually flow from the source region (upstream the double layer) down to the expanding region with a given flux Γ_0 (experimentally estimated). The positive ions then reach the bottom of the expanding chamber (at $r = R_2$) and exit with a reduced Bohm velocity due to high electronegativity (condition 4). The flux of negative ions at $r = R_2$ must be zero (condition 2) due to the small sheath around the expanding chamber walls. Finally, we consider that the negative ion velocity is nearly thermal when entering the double layer (condition 3).

Model results

We run the model for conditions fairly similar to the experimental results published by Plihon et al. [38]. We use the following parameters: $p = 1$ mTorr, $m_+ = 40$ uma (Ar^+), $m_- = 127$ uma (SF_5^-), $T_e = 3$ eV, $T_{\pm} = 0.2$ eV, $\nu_+ \approx 3.5 \times 10^4$ s $^{-1}$, $\nu_- \approx 2 \times 10^4$ s $^{-1}$, $\nu_i = n_g K_{i0} \exp(-E_{i0}/T_e)$, with $K_{i0} = 9.21 \times 10^{-14}$ and $E_{i0} = 19$ eV (SF_6 values, but really not important in the present calculation since most of the positive ions come from the source region), $\nu_a = n_g K_{a0}/(T_e^{1.2})$ with $K_{a0} = 1.55 \times 10^{-15}$ (this is about 20% of the value in SF_6),

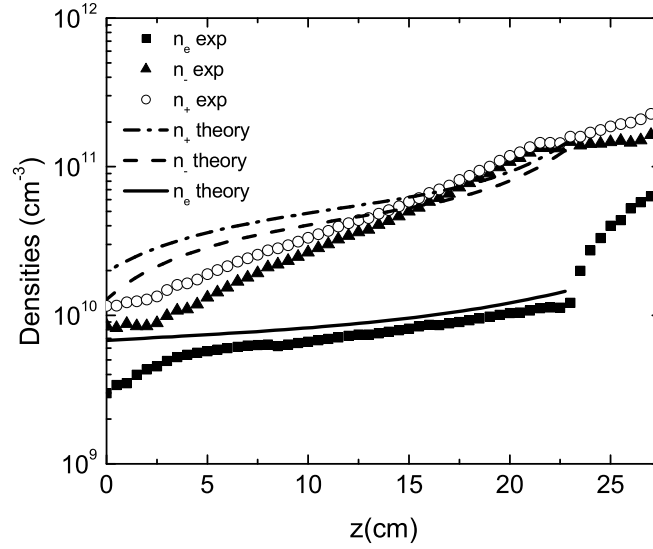


Figure 5.11: Densities in the expanding region

and finally $K_r = 3 \times 10^{-14} \text{ m}^3\text{s}^{-1}$. For the following calculation, we used the following boundary conditions:

$$\begin{aligned}\Gamma_+(r = R_1) &= n_0 u_B \\ \Gamma_-(r = R_2) &= 0 \\ u_+(r = R_2) &= 0.26 u_B \\ u_-(r = R_1) &= 0.26 u_B\end{aligned}$$

with $n_0 = 1.5 \times 10^{11} \text{ cm}^{-3}$ and $u_B \approx 2600 \text{ ms}^{-1}$.

Figure 5.11 shows the densities, and figure 5.12 shows α in the expanding region. The symbols stand for experimental results while the lines are the theoretical results. The altitude $z = 0$ on the figure corresponds to $r = R_2 = 4.5R_1$ in the calculation, and similarly $z \approx 22.5$ cm corresponds to $r = R_1 = 6.5$ cm. The agreement between theory and experiment is fairly good.

The model allows to estimate the velocities and the fluxes of both ion types, quantities that are difficult to measure. Figure 5.13 and 5.14 show the calculated ion velocities and ion fluxes respectively. The ions are always subsonic. The positive ion flux out of the source region exceeds by a fair amount the negative ion flux entering the source via the double layer. Therefore, the net thrust seems to be positive although it is reduced by about 25 % due to the negative ion back-flow.

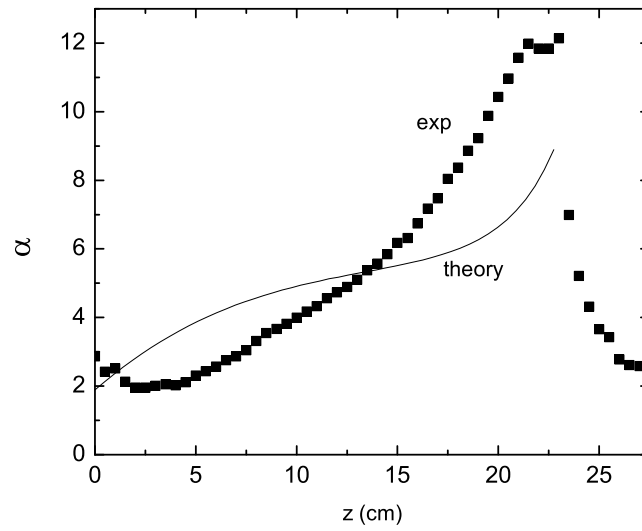


Figure 5.12: electronegativity in the expanding region

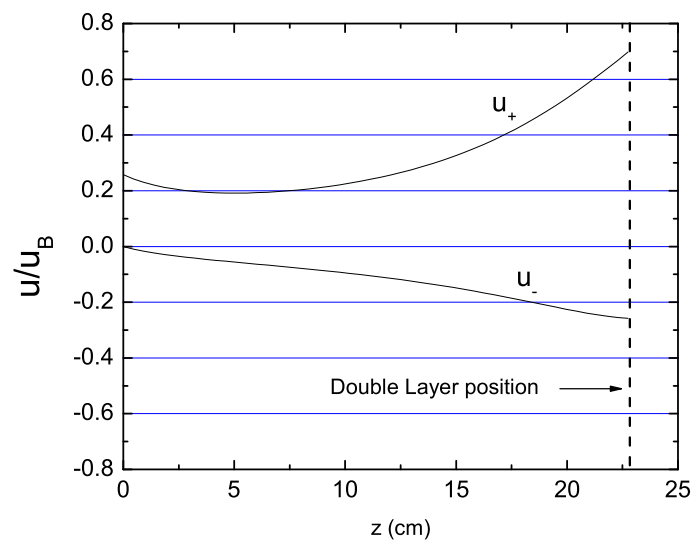


Figure 5.13: Ion velocities in the expanding region

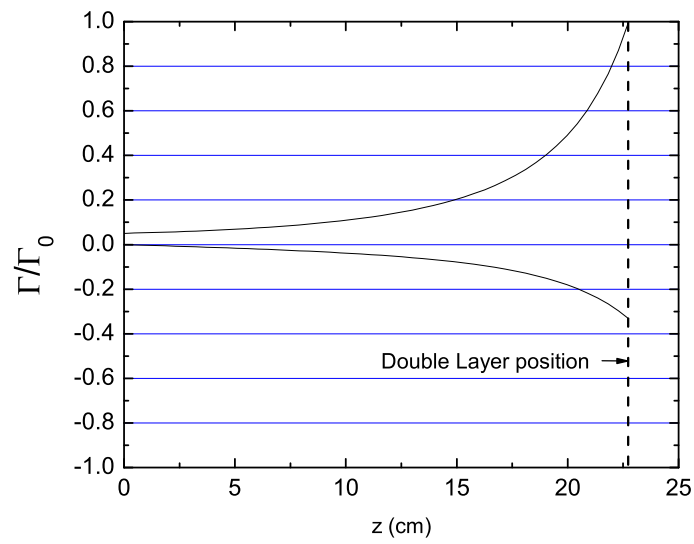


Figure 5.14: Ion fluxes in the expanding region

Chapter 6

Conclusions

The Helicon Double Layer Thruster (HDLT) concept, invented by Charles and Boswell at the Australian National University (ANU), has been investigated. The original concept (strongly diverging magnetic field in pure argon) has been tested in a helicon reactor installed at LPTP. The double layer has been found in the same parameter space as the Australian group. We have established that the DL does not necessarily need to be current free, since it was formed in a source having a dc connection to ground. This result is somewhat new and was not emphasized by the ANU group. The specific impulse and thrust derived from our flux and energy measurements are given below.

The effect of adding an electronegative gas as a possible improvement has also been investigated. In that case, the double layer was also easily formed, with or without magnetic field. However, the DL was unstable in a wide parameter range. A theoretical model has been developed to describe the upstream and downstream plasmas connected by the double layer. This model allows to estimate the net thrust provided by this concept. It appears that it is less promising than the HDLT concept.

6.1 Estimation of specific impulse and thrust

The specific impulse was calculated as follows:

$$I_s = \frac{1}{g_0} \sqrt{\frac{2q(V_{\text{beam}} - V_{\text{plasma}})}{M_+}} \quad (6.1)$$

where $V_{\text{beam}} - V_{\text{plasma}}$ is the potential drop across the DL, M_+ is the mass of argon ions, and g_0 is the gravity constant at sea level.

The thrust was calculated from the flux measured 7 cm below the DL, as follows:

$$T = \Gamma_{\text{beam}} S M_+ I_s g_0 \quad (6.2)$$

where Γ_{beam} is the flux of the beam out of the DL, S is the surface of the source exhaust.

Figures 6.1 (a), 6.2 (a) and 6.3 (a) show the specific impulse as a function of the three control parameters, i.e. pressure, power, and magnetic field respectively. The typical value of the specific impulse is around 800-900s, I_s being mostly independent of the magnetic field and the power, while increasing as the pressure decreases. This is due to the increase in the electron temperature when the pressure decreases.

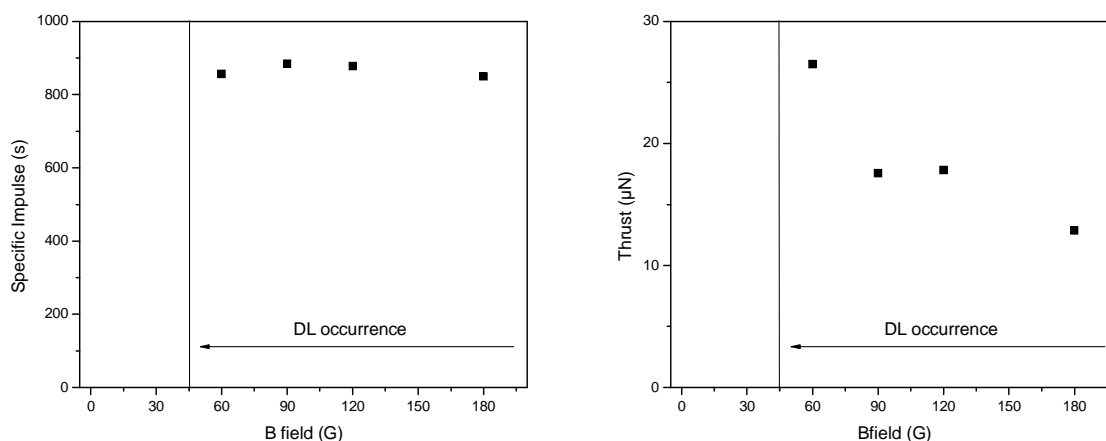


Figure 6.1: Specific impulse and Thrust as a function of magnetic, measured at $z = 20$ cm, for a 250 W power at 0.17 mT.

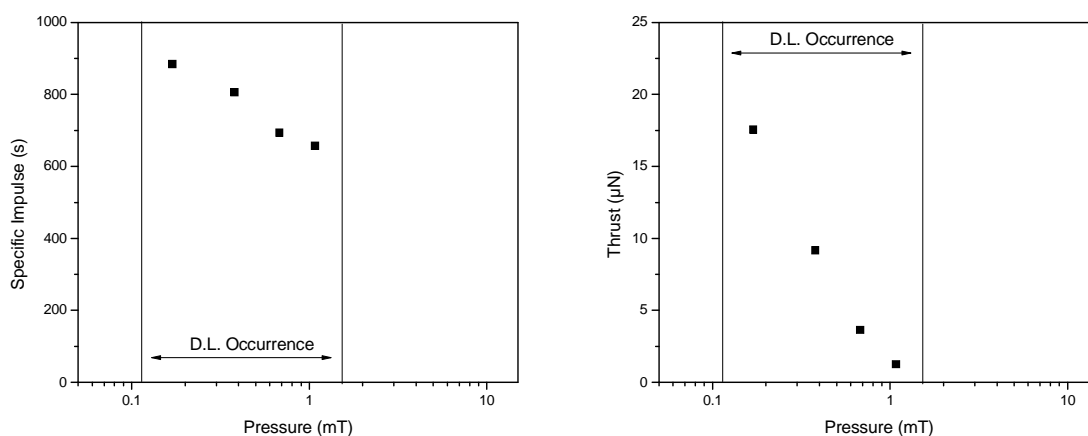


Figure 6.2: Specific impulse and Thrust as a function of pressure, measured at $z = 20$ cm, for a 250 W power and a 90 G magnetic field.

Figures 6.1 (b), 6.2 (b) and 6.3 (b) show the thrust for the same conditions. The thrust decreases if either the pressure or the magnetic field are increased. On the contrary, the thrust increases with the rf power, as expected. The thrust is rather low but could certainly be improved by optimizing the HDLT. We believe that by using Xenon and optimizing the ionization efficiency, the thrust could reach a few tens of mN for the same thruster size, i.e. $80\mu\text{N}/\text{cm}^2$. However, the specific impulse, which is already quite low, would be reduced.

The electronegative double layer concept provides even smaller thrust and specific impulse. Indeed, the voltage across the DL is lower, at least by a factor of 2 and the negative ion flux crossing the DL counter-flow reduces the efficiency by 25%.

The following table, summarizes the results obtained for a 600 W radiofrequency plasma.

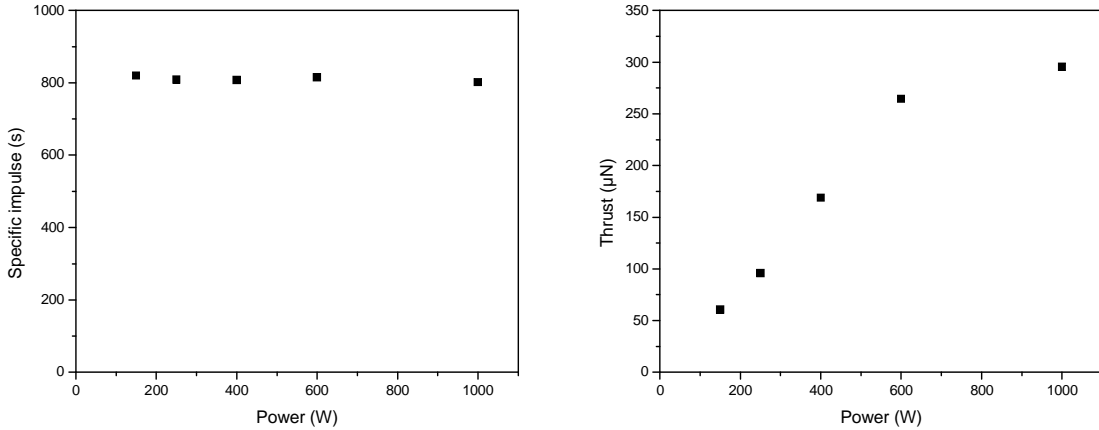


Figure 6.3: Specific impulse and Thrust as a function of power, measured at $z = 23$ cm, for a 90 G magnetic field at 0.2 mT.

	HDLT	ENDL
Thrust (mN)	0.3	0.05
Specific Impulse (s)	1000	500

Note that if all ions were accelerated away from the source in the axial direction (across the DL), the theoretical thrust would then be about 15 mN.

We conclude our study by the two following comments on the HDLT concept :

- The specific impulse cannot be varied significantly since it is intrinsically determined by the double-layer amplitude which is a weak function of the control parameters (magnetic field, gas pressure/flow, rf power)
- The thrust could probably be greatly improved by improving the source ionization efficiency (that is increase the input power and find the appropriate magnetic field for a maximum of helicon wave ionization). It seems possible since the double layer is robust, i.e. exists at high power.
- the crucial question for the scaling up to high power, apart from the typical thermal problems associated with it, is to check the maximum power at which the double layer still exists. As we do not have a good theoretical model of the phenomena, this cannot be predicted by now.
- Numerical simulations would be very useful to address these scaling up issues
- The main experimental work that remains to be done is to try to improve the DL amplitude by adding a dc-biased grid at the upper end of the tube. This may hopefully increase the potential in the source and therefore increase the potential difference between the upstream and the downstream plasma.

Bibliography

- [1] Christine Charles and Rod Boswell. Current-free double-layer formation in a high-density helicon discharge. Appl. Phys. Lett., 82:1356–1358, 2003.
- [2] C Charles. Hydrogen ion beam generated by a current-free double layer in a helicon plasma. Appl. Phys. Lett., 84:332–334, 2004.
- [3] Christine Charles and R W Boswell. Laboratory evidence of a supersonic ion beam generated by a current-free ”helicon” double-layer. Phys. Plasmas, 11:1706–1714, 2004.
- [4] Christine Charles. High source potential upstream of a current-free electric double layer. Phys. Plasmas, 12:044508, 2005.
- [5] Christine Charles. Spatially resolved energy analyzer measurements of an ion beam on the low potential side of a current-free double-layer. IEEE Transactions on plasma science, 33:336–337, 2005.
- [6] O Sutherland, C Charles, N Plihon, and R W Boswell. Experimental evidence of a double layer in a large volume helicon reactor. Phys. Rev. Lett., 95:205002, 2005.
- [7] Xuan Sun, Amy M. Keesee, Costel Biloiu, Earl E. Scime, Albert Meige, Christine Charles, and Rod W. Boswell. Observations of ion-beam formation in a current-free double layer. Phys. Rev. Lett., 95:025004, 2005.
- [8] Albert Meige, Rod W. Boswell, Christine Charles, and Miles M. Turner. One-dimensional particle-in-cell simulation of a current-free double layer in an expanding plasma. Phys. Plasmas, 12:052317, 2005.
- [9] Albert Meige, Rod W. Boswell, Christine Charles, Jean-Pierre Boeuf, Gerjan Hagelaar, and Miles M. Turner. One-dimensional simulation of an ion beam generated by a current-free double-layer. IEEE Transactions on plasma science, 33:334–335, 2005.
- [10] R.W. Boswell. Phys. Lett., 33A:470, 1970.
- [11] A. Cantin and R.R.R. Gagne. Appl. Phys. Lett., 30:31, 1977.
- [12] M.B. Hopkins and W.G. Graham. Rev. Sci. Instrum., 57:2210, 1986.
- [13] P. Chabert, T.E. Sheridan, R.W. Boswell, and J. Perrin. Plasma Sources Sci. Technol., 8:561, 1999.

- [14] T.E. Sheridan, P. Chabert, and R.W. Boswell. Plasma Sources Sci. Technol., 8:457, 1999.
- [15] S.G. Ingram and N.St.J. Braithwaite. Ion and electron energy analysis at a surface in a rf discharge. J. Phys. D: Appl. Phys., 21:1296, 1988.
- [16] C. Bohm and J. Perrin. Retarding field analyser for measurements of ion energy distributions and secondary electron emission coefficients in low pressure radio frequency discharges. Rev. Sci. Instrum., 64:31, 1993.
- [17] Amlie Perret. Effets de la frquence d'excitation sur l'uniformit du plasma dans les racteurs capacitifs grande surface. PhD thesis, Ecole Polytechnique, Palaiseau, France, June 2004.
- [18] A. Perret, P. Chabert, J. Jolly, and J.-P. Booth. Ion energy uniformity in high frequency capacitive discharges. Appl. Phys. Lett., 86(1):021501, 2005.
- [19] R.W. Boswell and F.F. Chen. Helicons-the early years. IEEE Transactions on plasma science, 25(6):1229–1244, December 1997.
- [20] F.F. Chen and R.W. Boswell. Helicons-the past decade. IEEE Transactions on plasma science, 25(6):1245–1257, December 1997.
- [21] R.W. Boswell P. Chabert and C. Davis. Investigation of an sf_6 helicon plasma. Journal of Vacuum Science and Technology A, 16(1):78–86, January 1998.
- [22] J. Perrin R.W. Boswell P. Chabert, N. Proust. High rate etching of $4h - sic$ using sf_6/o_2 helicon plasma. Applied Physics Letters, 76(16):2310–2312, April 2000.
- [23] P. Zhu and R.W. Boswell. Ar ii laser generated by landau damping of whistler waves at the lower hybrid frequency. Phys. Rev. Letters, 63(26):2805–2807, December 1989.
- [24] F.F. Chen. Plasma ionization by helicon waves. Plasma Physics and Controlled Fusion, 33(4):339–364, 1991.
- [25] R.W. Boswell. Measurements of the far-field resonance cone whistler mode waves in magnetoplasma. Nature, 258:58–60, November 1975.
- [26] R.W. Boswell A.W. Degeling, C. Jung and A.R. Ellingboe. Physics of Plasmas, 3:2788, 1996.
- [27] M.A. Lieberman and R.W. Boswell. Modeling the transitions from capacitive to inductive to wave-sustained rf discharges. J. Phys. IV France, 8:145–163, 1998.
- [28] R. Z. Sagdeev. Reviews of Plasma Physics. Number 23-91. 1966.
- [29] F. Verheest and M.A. Hellberg. Journal of Plasma Physics, 57:465, 1997.
- [30] R.N. Franklin and J. Snell. Journal of Plasma Physics, 64:131, 2000.
- [31] E. A. Bogdanov and A. A. Kudryavtsev. Technical Physics Letters, 27:905, 2001.

- [32] J. F. McKenzie and T. B. Boyle. New Journal of Physics, 5:26–1, 2003.
- [33] J. F. McKenzie. Journal of Plasma Physics, 69:199, 2003.
- [34] E. Infeld and G. Rowland. Nonlinear waves solitons and chaos. 2000.
- [35] S. Baboolal, R. Bharuthram, and M.A. Hellberg. Journal of Plasma Physics, 46:247, 1991.
- [36] F. Verheest. Physica Scripta, 47:274, 1993.
- [37] Fernando N. Gesto, Boyd D. Blackwell, Christine Charles, and Rod W. Boswell. Ion detachment in the helicon double-layer thruster exhaust beam. J. Prop. Power, page accepted, 2005.
- [38] N. Plihon, C.S. Corr, and P. Chabert. Appl. Phys. Lett., 86:091501, 2005.
- [39] N. Plihon, C.S. Corr, P. Chabert, and JL Raimbault. J. Appl. Phys., 98:023306, 2005.
- [40] J.G. Andrews and J.E. Allen. Proc. Roy. Soc., A320:459, 1971.